Technical Design Report
for the
Paul Scherrer Institute Experiment R-12-01.1: Studying the Proton "Radius" Puzzle with μp Elastic Scattering
March 19, 2014

The MUon proton Scattering Experiment collaboration (MUSE):

R. Gilman (Contact person),[1] E.J. Downie (Spokesperson),[2] G. Ron (Spokesperson),[3] A. Afanasev,[2] J. Arrington,[4] O. Ates,[5] C. Ayerbe-Gayoso,[6] F. Benmokhtar,[7] J. Bernauer,[8] E. Brash,[9] W. J. Briscoe,[2] K. Deiters,[10] J. Diefenbach,[5] B. Dongwi,[5] L. El Fassi,[1] S. Gilad,[8] K. Gnanvo,[11] R. Gothe,[12] D. Higinbotham,[13] Y. Ilieva,[12] M. Jones,[13] M. Kohl,[5] G. Kumbartzki,[1] J. Lichtenstadt,[14] A. Liyanage,[5] N. Liyanage,[11] Z.-E. Meziani,[15] P. Monaghan,[5] K. E. Mesick,[1] C. Perdrisat,[6] E. Piasetzsky,[14] V. Punjabi,[16] R. Ransome,[1] D. Reggiani,[10] P. Reimer,[4] A. Richter,[17] A. Sarty,[18] Y. Shamai,[19] N. Sparveris,[15] S. Strauch,[12] V. Sulkosky,[20] A.S. Tadepalli,[1] M. Taragin,[21] and L. Weinstein[22]

[1]*Rutgers University, New Brunswick, New Jersey, USA*

[2]*George Washington University, Washington, DC, USA*

[3]*Hebrew University of Jerusalem, Jerusalem, Israel*

[4]*Argonne National Lab, Argonne, IL, USA*

[5]*Hampton University, Hampton, Virginia, USA*

[6]*College of William & Mary, Williamsburg, Virginia, USA*

[7]*Duquesne University, Pittsburgh, PA, USA*

[8]*Massachusetts Institute of Technology, Cambridge, Massachusetts, USA*

[9]*Christopher Newport University, Newport News, Virginia, USA*

[10]*Paul Scherrer Institut, CH-5232 Villigen, Switzerland*

[11]*University of Virginia, Charlottesville, Virginia, USA*

[12]*University of South Carolina, Columbia, South Carolina, USA*

[13]*Jefferson Lab, Newport News, Viginia, USA*

[14]*Tel Aviv University, Tel Aviv, Israel*

[15] *Temple University, Philadelphia, Pennsylvania, USA*
[16] *Norfolk State University, Norfolk, Virginia, USA*
[17] *Technical University of Darmstadt, Darmstadt, Germany*
[18] *St. Mary's University, Halifax, Nova Scotia, Canada*
[19] *Soreq Nuclear Research Center, Israel*
[20] *Longwood University, Farmville, Virginia, USA*
[21] *Weizmann Institute, Rehovot, Israel*
[22] *Old Dominion University, Norfolk, Virginia, USA*

The difference in proton radii measured with μp atoms and with ep atoms and scattering remains an unexplained puzzle. The PSI MUSE proposal is to measure $\mu^{\pm}p$ and $e^{\pm}p$ scattering in the same experiment at the same time. The experiment will determine cross sections, two-photon effects, form factors, and radii independently for the two reactions, and will allow μp and ep results to be compared with reduced systematic uncertainties. These data should provide the best test of lepton universality in a scattering experiment to date, about an order of magnitude improvement over previous tests. Measuring both particle polarities will allow a test of two-photon exchange at the sub-percent level, about a factor of four improvement on previous low momentum transfer determinations, and similar to the current generation of higher momentum transfer electron experiments. The experiment has the potential to demonstrate whether the μp and ep interactions are consistent or different, and whether any difference results from novel physics or two-photon exchange. The uncertainties are such that if the discrepancy is real it should be confirmed with similar significance as already established between the regular and muonic hydrogen Lamb shift.

CONTENTS

I. MOTIVATION

The proton radius was thought reliably determined to be ≈0.88 fm for several years, by atomic hydrogen and *ep* scattering measurements. The hydrogen atom experiments led, in the 2006 CODATA analysis [1], to $r_p = 0.8768 \pm 0.0069$ fm. The electron-proton scattering analysis gave $r_p = 0.895 \pm 0.018$ fm in the analysis of [2], which discussed the needed Coulomb corrections and choice of an appropriate parameterization to fit form factor data. This situation changed in summer 2010 when a Paul Scherrer Institute (PSI) experiment [3] reported that the radius determined from muonic hydrogen level transitions is 0.842 ± 0.001 fm, about 5σ off from the nearly order of magnitude less precise non-muonic measurements. We refer to this situation as the proton radius puzzle.

The proton radius puzzle has been an active field for research, with many theoretical studies proposing possible explanations, new experimental results, and reanalyses of data. In the interest of brevity, here we point out the following:

- The precise electron scattering cross section measurement [4] at Mainz that yielded 0.879 ± 0.008 fm.
- The Jefferson Lab polarization measurement [5], that combined with non-Mainz world data reanalysis yielded 0.870 ± 0.010 fm.
- The CODATA2010 [6] analysis that included the Mainz data and reconfirmed the puzzle.
- The 2013 muonic hydrogen measurement [7], in agreement with the 2010 PSI measurement.
- A review paper in Annual Review of Nuclear and Particle Science [8].
- The z-expansion reanalysis of Hill and Paz [9, 10].

Of the many possible explanations of the proton radius puzzle, almost all are considered to be wrong by the overwhelming majority of the community. The remainder are probably best characterized as not ruled out, but having, at best, minority support. It is important to note that there are three outstanding problems – the proton radius puzzle, the muon

$g-2$ discrepancy, and the cosmic positron excess – any or none of which might be real indications of new physics, and which all are important for constraining new physics. Following are some possible explanations of the radius puzzle.

- *Beyond Standard Model physics.* Several examples exist. In [11], the possibility of a new $U(1)_R$ gauge symmetry is discussed, which leads to different μp and ep interactions. A proposed test is enhanced parity violation in μp scattering, orders of magnitude enhanced from the expected parity violation from Z^0 exchange. Ref. [12] points out that this model involves a new vector gauge boson with mass around tens of MeV, which could be radiated from muons. The lack of observation of such a boson in, *e.g.*, $K \to \mu\nu$ severely constrains such models. Carlson and Rislow [13, 14] have studied how fine tuning couplings of new scalar + pseudoscalar or vector + axial vector forces allows current limits to be evaded, and implications for kaon decays. Tucker-Smith and Yavin [15] studied how the puzzle could be explained by a new ≈MeV mass scalar or vector particle, with implications for the muon $g-2$ discrepancy. Also note that a new light force particle could cause a "break" in the form factor at $Q^2 \approx m^2$.

- *Novel two-photon exchange effects.* Miller [16] has proposed a proton polarizability correction proportional to m_l^4, which would be important for the muonic hydrogen radius but which would not affect electronic systems. The mechanism leads to enhanced two-photon exchange effects in muon-proton scattering, which can be experimentally tested.

- *Unexpected aspects of proton structure.* There are a number of suggestions of structures in the form factors from hadronic physics, or anomalously large Zemach radii. None are accepted.

- *Different radii.* There are a number of suggestions that the atomic and scattering experiments measure different radii, or radii in different frames. But in both atomic and scattering measurements, the experiments measure the slope of the form factor, which is a relativistic invariant.

- *Issues in ep scattering:* A number of issues have been raised concerning the electron scattering radius extractions. Here we refer to [8] and state our conclusion that the more flexible fits are superior, and all determine a larger proton radius.

New physics might violate lepton universality, so we note that this has been tested crudely in earlier scattering measurements at the 5 – 10% level. Additional tests include nuclear radii. Measurements of muonic deuterium and helium-4 are underway, and old measurements of muonic ^{12}C [17] are consistent with electron scattering [18]: $\langle r^2\rangle^{1/2} = 2.483 \pm 0.002$ fm vs. 2.478 ± 0.009 fm. It could be that issues at the nucleon level are washed out at the larger nuclear radii, effects in the proton and neutron lead to cancellations, or unappreciated uncertainties in extractions of nuclear radii exist – polarizability corrections will generally be much larger due to low lying excited states.

Finally, we note that two-photon exchange effects were studied in μp elastic scattering. No effects were seen [19] for differences in $\mu^+ p$ vs. $\mu^- p$ elastic scattering, but the uncertainties of 4 – 30% exceed modern estimates of the two-photon effect. Also, Rosenbluth separations determined to ≈4% showed no visible nonlinearities, but again the uncertainties exceed modern estimates of effects at the ≈1% level.

In *ep* scattering, the radius is determined from the slope of the form factor at $Q^2 = 0$. Here we consider the Mainz *ep* data in more detail, as it is related to the measurements that we will propose. Figure 1 shows an indication of the proton radius from the Mainz data set, showing $G_E^p(Q^2)$ extracted from the cross sections using spline and polynomial fit functions to the data. The lowest Q^2 points are more consistent with the larger radius found in *ep* experiments, but even before 0.02 GeV^2 the form factor is starting to show nonlinearities. The Kelly parameterization [20] generally predicts the trends of the data. The curvature at low Q^2 indicates the importance of measuring at low Q^2 to be sensitive to the radius, and over a range of Q^2 to have sensitivity to higher-order terms.

To summarize the situation, we quote from the Particle Data Group [21]: "Most measurements of the radius of the proton involve electron-proton interactions, and most of the more recent values agree with one another... However, a measurement using muonic hydrogen finds $r_p = 0.84184(67)$ fm, which is eight times more precise and seven standard deviations (using the CODATA 10 [6] error) from the electronic results... Until the differ-

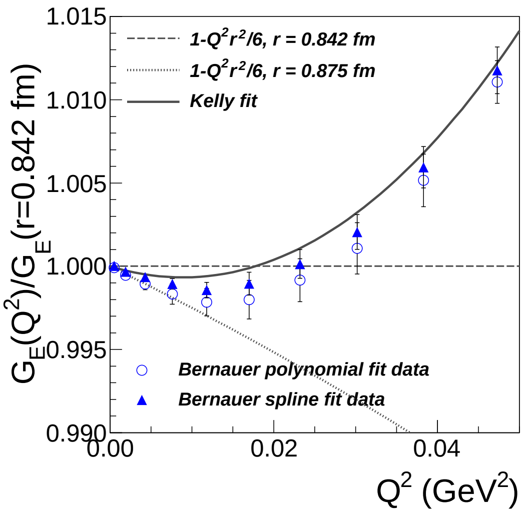

FIG. 1. Mainz results for the proton electric form factor determined by spline and polynomial fit analyses of the cross sections, along with the Kelly parameterization and a linear fit assuming the radius determined by *ep* measurements, relative to expectations from a linear fit using the radius determined from μp atoms.

ence between the *ep* and μp values is understood, it does not make much sense to average all the values together. For the present, we stick with the less precise (and provisionally suspect) CODATA 2010 value. *It is up to workers in this field to solve this puzzle.*" (Emphasis added.)

The resolution of the proton radius puzzle remains unclear. The puzzle is being investigated with a range of new muonic atom experiments already underway, atomic hydrogen experiments that will likely take the next several years, and very low-Q^2 electron scattering experiments that have already started. Here we discuss the PSI MUSE measurement, which aims to measure elastic μp and *ep* scattering with both charge signs. Our intent is

- to directly compare *ep* to μp at the percent level, more precisely than done before,
- to compare scattering of positive vs. negative charged particles to test two-photon exchange effects in both reactions at the percent level, more precisely than done before,
- and to extract radii from both reactions, which will be the first μp scattering radius

determination, at roughly the same level as done in previous scattering experiments.

II. EXPERIMENT OVERVIEW

MUSE will measure cross sections for elastic $\mu^{\pm}p$ and $e^{\pm}p$ scattering in the PSI πM1 beam line. In this section we will give an overview of the beam, equipment, background reactions and rates, and uncertainties.

A. Beam Properties

The πM1 channel transports mixed beams of electrons, muons, pions, and protons generated by interactions of the 50 MHz primary proton beam at the M1 production target. The channel momentum range is $\approx$100 − 500 MeV/c, but the MUSE experiment only uses beam momenta of $\approx$ 115, 153, and 210 MeV/c, at which no protons are seen. These momenta are chosen as they provide a good flux of muons and a good RF time separation between the different particles, as shown in Fig. 2: 3 − 6 ns separation, compared to the intrinsic width in time of $\approx$300 ps. More details regarding the properties of the beam are given in Section III A.

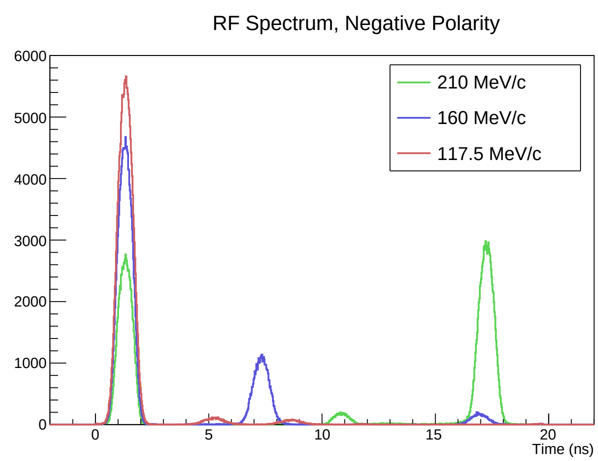

FIG. 2. Measured RF time spectrum for −117.5 MeV/c, −160 MeV/c, and −210 MeV/c at a distance of 23.5 m from the production target. The peaks from left to right are e, π, μ for −117.5 MeV/c and −160 MeV/c, and e, μ, π for −210 MeV/c. Absolute scale is arbitrary, while the relative area of the peaks indicates the relative particle fractions versus momentum.

The channel also transports "background" particles which cannot be seen in Fig. 2 as they are at a level about 2 orders of magnitude below the electrons, muons, and pions. The primary background is muon tails in the RF time that arise from near 0 (180) degree decay of lower (higher) momentum pions in the first several meters of the πM1 channel, before the first dipole. In the region of the target there is also a large beam halo of muons from pion decay – the pion decay rate at our momenta is about 10%/m – and a small beam halo of electrons from muon decay – the muon decay rate at our momenta is about 0.1%/m. Section II C discusses how these backgrounds are handled.

The total flux in the channel can be as large as a few hundred MHz, but will be limited by a collimator at the intermediate focus point (IFP) to $\approx$5 MHz at the target. The beam dispersion at the intermediate focus is 7 cm/%, so collimation reduces the momentum spread of the beam.

B. Equipment

Figure 3 shows the planned experimental setup. Test measurements show that beam particle type and momentum can be determined through timing measurements at the intermediate focus point of the channel and near the target position. These measurements will be done by a combination of Scintillating Fiber (SciFi) and sapphire beam Cerenkov detectors. The SciFi detectors are discussed in Section III B 2. The beam Cerenkovs are discussed in Section III B 1.

Because of the spot size and angular divergences, and tails to the beam, it is necessary to track particles into the target, which we do with GEM chambers. See Section III B 3 for a detailed GEM description. We are also planning to implement a small annular veto scintillator around the beam just upstream of the target to help suppress triggers from particle decays in flight, particles scattering from the upstream beamline elements, and interactions with the scattering chamber.

After the GEM chambers, particles enter the vacuum chamber and can scatter from the liquid hydrogen target or from windows in the system. Detailed target design awaits a thorough characterization of the beam properties, measured with the GEM chambers, and ensuing simulations. The intent is to minimize scattering of halo particles in thick walls,

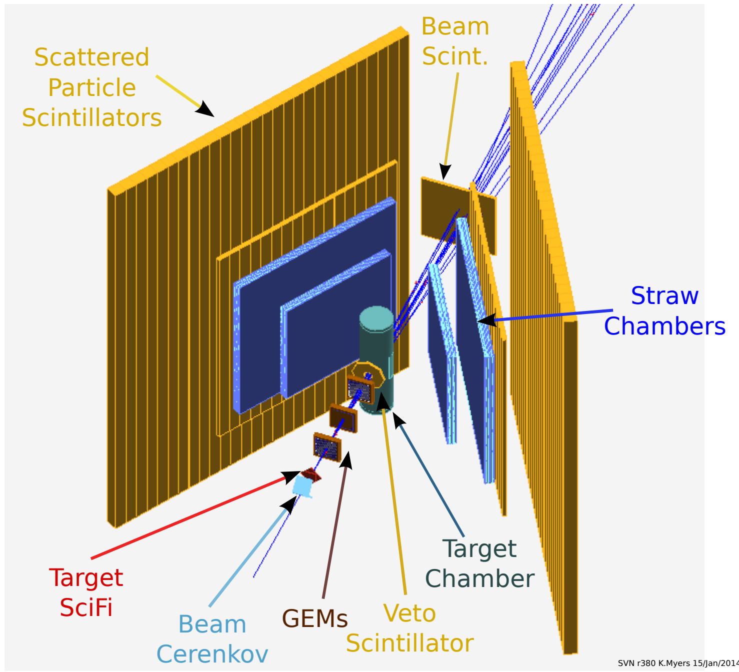

FIG. 3. Geant4 cartoon of the experimental systems in the πM1 area. Along the beam line is the beam Cerenkov, the Scintillating Fiber detector, three GEM chambers, the veto scintillator, the cryotarget, and the beam monitor scintillators. Scattered particles are detected by two identical spectrometers, each with two straw chambers and two planes of scintillator paddles.

which might generate a large trigger rate, while minimizing multiple scattering of beam particles of interest in the hydrogen cryotarget. Section III C describes the cryotarget in more detail.

Particles that scatter left or right in the target region are detected in one of two identical detector systems, consisting of straw chambers to determine the scattered trajectory – see Section IV A – and two planes of high-precision scintillators to trigger the DAQ and determine RF times and energy loss in the scintillators – see Section IV B. The two identical systems double the statistical precision of the experiment, and give simultaneous but independent cross section measurements that provide an overlap and check of some of the experiment systematics.

A high-precision beam monitoring scintillator hodoscope will be positioned downstream of the target to monitor the RF timing of beam particles and thus beam stability. While scattered particles that trigger the event readout do not pass through the beam scintillator, there is about 1 random coincident beam particle every 200 ns, which can be used to monitor the beam flux and RF timing of the particles.

The triggering will be effected by an FPGA system, described in Section V A, to combine signals from scintillator paddles and beam line detectors to determine if there is a scattered particle associated with a beam e or μ. The data acquisition system, described in Section VI, uses standard readout technology of modules in VME crates, but with the exception of recently developed TRB3 system with frontend PADIWA boards for discrimination and TDC signals.

We emphasize at this point that all detector and DAQ components and the target use existing, often standard technologies. The scintillating fiber arrays are standard technology. The beam Cerenkov is based on a Fermilab prototype. The GEM chambers were previously used in the OLYMPUS experiment. Numerous hydrogen cryotargets exist. The scattered particle chambers are based on the PANDA design. The high-precision scintillators copy and adapt a system developed and built for the Jefferson Lab 12-GeV upgrade. The DAQ uses existing technology. To a large degree the individual components are also being built by groups with experience in building these devices in the past. The novel feature of this experiment is assembling relatively modern high-rate detectors to measure a high-precision lepton scattering cross section in the PSI πM1 beam line.

C. Physics Reactions and Backgrounds

Backgrounds are a problem if it is hard to separate the background reactions from the reactions of interest, if backgrounds generate high trigger rates that lead to high DAQ dead time, or if backgrounds cause high singles rates that make it hard to analyze events.

The beam-induced background processes include the following:

- For incident μ's: scattering from the target end windows, decaying in flight, and knocking out δ's from the target. The rates for elastic muon scattering and some background reactions are shown in Fig. 4. The ratio of rates for elastic μ scattering from carbon and aluminum versus hydrogen are shown in Fig. 5, which illustrates the advantage of using a kapton[1] target cell rather than an aluminum target cell.

[1] Kapton is $C_{22}H_{10}N_2 0_5$.

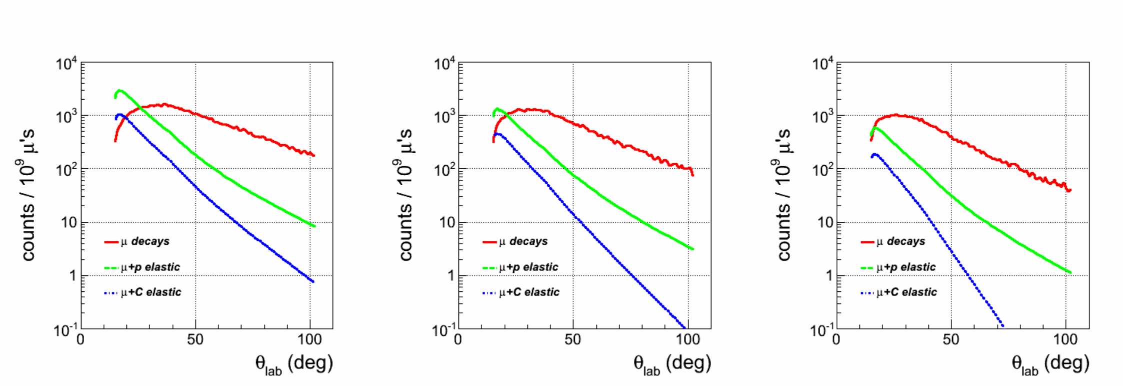

FIG. 4. Estimated rates at 115 MeV/c (left), 153 MeV/c (middle), and 210 MeV/c (right) as a function of angle for muon elastic scattering from protons and from carbon in the target end caps, and for electrons from muon decays in flight in a 10 cm region near the target. The counts shown are based on the detector geometry, 1° angle bins, and 10^9 incident μ's, corresponding to about 1 hour of data. The wiggles in the muon decay rate are due to use of a numerical simulation in this case to generate rates. Elastic scattering rates fall faster with angle or energy than does the muon decay rate.

At the trigger level, the use of coincident scintillator paddles will provide some directionality that suppresses muon decays by ensuring that events come from the target region. The e's from μ decay have a wide range of angles due to the 3-body nature of the decay, and at the trigger level resemble scattering events for decays near the target. A simple simulation of the μ decay kinematics is shown in Fig. 6. At the analysis level muon decay events can be removed by time of flight, and all backgrounds can be subtracted using dummy target comparisons.

- For incident e's: scattering from the target end windows, Moller and Bhabha scattering from atomic electrons, and positron annihilation. Dummy target subtraction removes the end window background. Large-angle Moller and Bhabha electrons and positrons are low in momentum and should not trigger our system. Positron annihilation generates photons that we are inefficient at detecting. Note that radiative corrections are much more important for electrons and positrons than for muons.

- For incident π's: all processes are backgrounds. At the trigger level, pion-induced events are suppressed by determining beam particle identification (PID) with beam

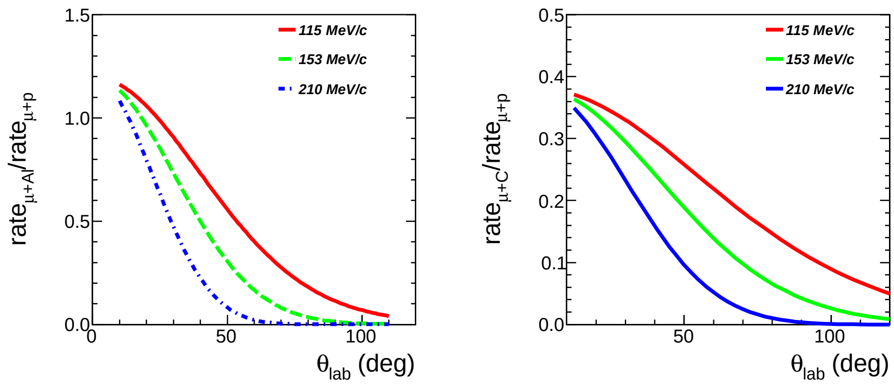

FIG. 5. Ratio of rates for elastic μp scattering for aluminum (left) and carbon (right) relative to hydrogen as a function of angle and beam energy. The thicknesses of the materials were 250 μm for C, 200 μm for Al, and 4 cm for H. Nuclear elastic rates are enhanced by Z^2 but suppressed by a faster fall off of the form factors with Q^2. Background from kapton is about 3 times smaller than background from aluminum.

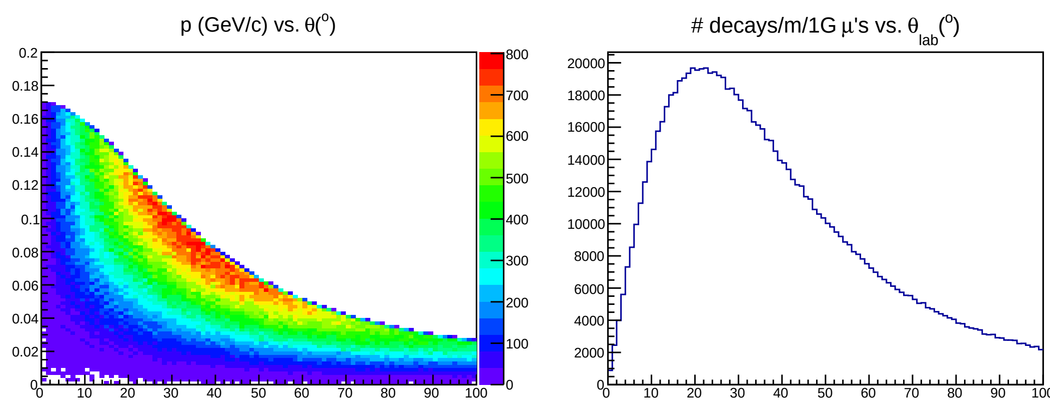

FIG. 6. Left: Simulation of e momentum vs. angle for decays in flight of 153 MeV/c unpolarized μ's. Right: A projection showing the angular distribution of the electrons from muon decays. The distribution shifts slightly to smaller or larger angles depending on muon polarization direction. The numbers of electrons are per meter of flight path and per 10^9 incident μ's.

line detector timing.

Section VIII A describes in more detail estimated uncertainties resulting from removing backgrounds through cuts and subtractions.

Singles and trigger rates are presented in Table I for all kinematic settings. Elastic scattering is calculated from measured form factors, and singles and trigger rates from all processes are estimated with GEANT4 simulations. The estimates use beam fluxes given in Table III in Section III A, the detector configuration shown in Fig. 3, and a 4 cm thick LH_2 target, with 0.125 mm thick kapton entrance and exit windows. The trigger rates are based on sufficient energy being deposited in two planes of scintillator paddles, no hit detected in the veto scintillator, and, for the π's, the efficiency of the beam PID system at rejecting π events at the trigger level – see Section V B. The singles rate is the integrated rate for all scintillator paddles in a wall, which is dominated by forward-angle particles, with the most forward scintillator paddle having up to about one-third of the total rate quoted. Background rates that were cross checked with standalone estimates include $\pi^{\pm}p$ scattering, evaluated using the SAID partial wave analysis, available online at `http://gwdac.phys.gwu.edu/`, and particle decays in flight.

TABLE I. Rates for both detector arms combined for various processes in Hz (or kHz) with the estimated beam fluxes totaling 5 MHz for all particle types. The "+(-)" momenta indicate positive (negative) polarity particles. For elastic processes from the target the singles and trigger rates are basically equal, but for particles from decays in flight or low-energy particles knocked out of the target this is not the case. The rates are for both detector arms combined.

Momentum (MeV/c)	+115	+153	+210	-115	-153	-210
$\mu + p$ **elastic scattering**	**0.6**	**2.6**	**1.0**	**0.3**	**0.7**	**0.5**
μ+kapton elastic scattering	0.8	2.0	0.4	0.4	0.5	0.2
Geant4: μ singles	655	1.8k	1.3k	335	440	684
Geant4: μ triggers	57	241	111	29	61	56
$e + p$ **elastic scattering**	**54**	**20**	**1.9**	**55**	**28**	**7.5**
e+kapton elastic scattering	21	6.6	0.5	22	9.5	2.0
Geant4: e singles	139k	84.6k	16.4k	158k	134k	69.3k
Geant4: e triggers	3.0k	2.3k	635	3.6k	3.7k	2.7k
Geant4: π singles	12.7k	176k	227k	6.4k	48.0k	137k
Geant4: π triggers	1.8k	28.6k	33.8k	896	7.9k	20.4k
Geant4: π triggers + beam PID	15.2	277	6.8	7.3	76.3	4.1
Total singles rate	152.3k	262.2k	245.0k	164.9k	182.7k	206.9k
Total Geant4 triggers + beam PID	3.1k	2.9k	756	3.7k	3.9k	2.8k

The Geant4 triggers in Table I exceed the elastic triggers, mainly from interactions with the upstream beam line detectors scattering particles straight into the scintillators to generate a trigger. At the analysis level these events can easily be separated from the events that are generated closer to the target. The highest DAQ rate is $\approx$ 4 kHz, a factor of 2 higher than our desired DAQ rate. We are working on optimizing the veto scintillator design to reduce the non-vetoed trigger rate further. Our goal is for the DAQ system to be able to read out an event in 0.15 ms, which would lead to 30% dead time at 2 kHz. A straightforward upgrade of the MIDAS DAQ implementation we used in test runs should be able to reduce our current read out time of 0.4 ms to 0.15 ms, simply by using block transfers for the QDCs. The GEM readout requires more work, and is discussed in Section III B 3. If dead time is too high and / or the DAQ rate too high, contingency plans include prescaling forward-angle events, where both signal and background rates are higher, prescaling electron events, which are much more numerous than muon events, and more beam time at settings with the highest dead times.

The highest total background singles rate is about 270 kHz, so contamination of the scattered event analysis with other particles is at the 3% level, assuming a 100 ns time window, which is the scale of straw chamber drift times, but about 0.6% for being in the same RF bucket, the appropriate scale for the scintillators. Due to the large number of elements in the scattered particle scintillators and straw chambers, these backgrounds should not be a significant problem. The most significant random background is the 10% probability of a second beam particle in the same RF bucket as the triggering beam particle. At the analysis level, time resolution is sufficient to identify the triggering beam particle, except for two beam particles of the same type in the same beam pulse. But at the trigger level it will be difficult to identify which particle is the triggering particle. Thus, if one of the particles is a pion, which have a much larger scattering cross section, the event cannot be read out without swamping the DAQ with pion scattering events.

D. Uncertainties

Figure 1 showed that the effect of the difference in the proton radius being 0.84 fm vs. 0.88 fm in the low Q^2 region up to ≈ 0.06 GeV^2 in which the form factor falloff is most sensitive to the linear term is small, at the percent level or below in the form factor, and twice as much in the cross section. Also note that conventional two-photon effects are estimated to be tenths of a percent in the proposed kinematics. In MUSE we combine a low-flux beam from πM1 with a large solid-angle detector to obtain precise relative cross sections at the sub-percent level.

The planned statistical precision of MUSE is $\approx$1% in our lowest precision bins, and well below 1% in most of our kinematic range. Estimated relative systematic uncertainties are at the few tenths of a percent level. Sub-percent level absolute uncertainties, which are needed if one is to use absolute cross sections, are not achievable. The systematic uncertainties will be verified by measuring multiple cross sections with 6 primary experiment settings – two beam polarities $\times$ three beam momenta – with the large solid-angle detector acceptance subdivided into numerous bins. These primary settings will be supplemented with additional measurements at offset angles and momenta.

Cross section, form factor, and radius comparisons will use the data subsets cross-normalized to each other and to the $Q^2 = 0$ value of the form factor. This will allow electron vs. muon comparisons about an order of magnitude better than previous measurements, positive to negative beam polarity comparisons at about the level of conventional two-photon effects, and radius extractions with similar precision to previous extractions.

The number of counts measured is related to the cross section by

$$N_{counts} = N_{beam} \times (x\rho)_{target} \times \frac{d\sigma}{d\Omega} \times \Delta\Omega \times \epsilon \ , \tag{1}$$

where N_{counts} is the number of elastic events counted, N_{beam} is the number of beam particles, $(x\rho)_{target}$ is the target areal density, $\frac{d\sigma}{d\Omega}$ is the elastic differential cross section, $\Delta\Omega$ is the detector solid angle, and ϵ accounts for all efficiency factors (detection, electronic, data acquisition, and analysis efficiencies) and radiative corrections.

Table II summarizes the relative systematic uncertainties of the measurement, many of which are evident from the cross section calculation with Eq. 1. Efficiencies of detectors that measure beam properties – flux, particle type, or trajectories – can affect the number of counts but are independent of the scattering angle, so uncertainties do not contribute to relative cross section systematics. The factors N_{beam} and $(x\rho)_{target}$ are the same independent of scattering angle, so the relative uncertainty vanishes. The target density ρ_{target} will

TABLE II. Summary of relative systematic uncertainties on the cross section. The Total uncertainty results from adding the estimated individual uncertainties in quadrature. Items marked with a dash have very small systematic uncertainties, while items marked with TBD are expected to be small, but are hard to evaluate without the data in hand.

Systematic	Relative Uncertainty (%)
beam line detector efficiency	–
beam flux	–
target thickness	–
solid angle	0.1
scintillator efficiency	0.1
straw chamber efficiency	–
analysis uncertainties	TBD
detector stability	TBD
beam momentum sensitivity	0.1
angle determination	0.1
multiple scattering	0.3
radiative corrections - muons	0.1
radiative corrections - electrons	0.5
magnetic contributions	0.1
data set normalization	–
Total - muons	0.4
Total - electrons	0.6

come in as a higher-order correction, primarily as particles scattering at different angles go through different amounts of the target, with different amounts of multiple scattering that averages over kinematics. The solid angle $\Delta\Omega$ is determined by the precision of the wire chambers. As $\Delta\Omega = dA/r^2 = (dxdy)/r^2$, the relative uncertainties add in quadrature. Since reconstruction resolutions do not change the solid angle, what is important is that the chamber wire positions need to be determined precisely. We plan to determine wire positions at the $\approx$25 μm level, compared to $\approx$2.5 cm wide bins, so that relative solid angle uncertainties are at the 0.1% level. The detector system is designed for high detection efficiency, so that the angle-to-angle variation is below the tenths of a percent level. (At larger angles statistics will limit our ability to know the efficiency.) Scintillator thresholds will be calibrated with ADC spectra checked against simulations, with resulting uncertainties estimated to be $< 0.1\%$. Trigger programming will have to be carefully studied to ensure that it does not introduce paddle-dependent efficiencies. Tracking efficiencies should be $\approx$100% due to the use of redundant chamber planes. The analysis uncertainties relate to how sensitive the result is to cuts, and how resolutions, backgrounds, and noise lead to uncertainties in the results. As an example, effects of electronic backgrounds from ground loops and the resulting uncertainties are hard to estimate in advance of setting up the experiment. At the planned level of uncertainties for MUSE, another major concern and potentially the limiting factor related to the equipment is the detector stability. This will be monitored and estimated by studying run-to-run stability of efficiencies and cross sections, but it is hard to estimate in advance the detector stability and its uncertainty.

Not evident in Eq. 1 is that the cross section varies with beam momentum and scattering angle, so offsets in these can lead to changes in the cross sections that vary with angle. Offsets in beam energy, E, change the scattering kinematics and factors of E, E', and Q^2 that go into the cross section formula, and lead to the form factor being determined at the wrong Q^2. Figure 7 shows the sensitivity of the measured cross sections to offsets in the beam energy and to averaging over the πM1 momentum acceptance.

For the planned kinematic coverage of $20^\circ - 100^\circ$, both effects act roughly as overall normalization offsets. The beam momentum can be determined at the $\approx 0.1 - 0.2\%$ level through the differences in RF time of the different particle types at the target and through time of flight between the detectors at the IFP and at the target. The measured beam momenta must then be corrected by simulation for energy losses in materials to the momenta at the scattering vertex. As the data will be renormalized in the end, the important issue is the angle-to-angle variations in Fig. 7, which are well below 0.1%. We conclude that the beam momentum sensitivity of the relative cross sections is small. Section VIII C 2 provides more detail including a more realistic (Geant simulated) beam momentum spectrum, but the conclusions are unchanged.

Figure 8 shows that offsets in the scattering angle change the cross section, which changes the slope of the form factor vs. Q^2 and the radius. Section VII describes how to determine the spectrometer angles to $\approx$0.2 mr with dedicated calibration data. We use a

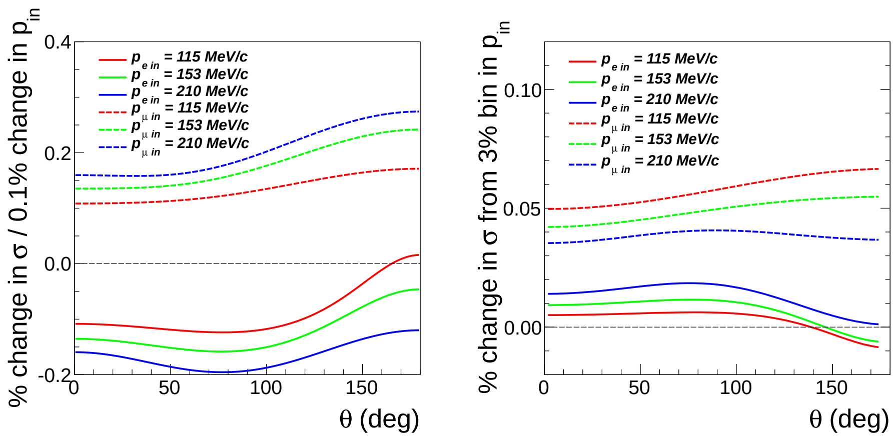

FIG. 7. Left: Change in cross section in percent for a 0.1% change in the beam momentum. Right: Change in cross section in percent when averaging over a ±1.5% bin in the beam momentum. We assumed a uniform distribution in incident momentum, and evaluated the average cross section for the full momentum bin compared to the cross section for a mono-energetic beam at the central momentum. Both studies used the Kelly form factor parameterization [20].

special calibration measurement with precisely rotated chambers to determine the angle, and check the calibration using the symmetric spectrometers on both sides of the beam, as well as a special offset angle measurement. The angle offset effect should be below 0.2%, with a relative uncertainty at the 0.1% level.

Figure 8 also shows the effect of multiple scattering, which in effect averages over scattering angles. If ignored, multiple scattering after renormalization of the data leads to a smaller radius. For a fixed system, the multiple scattering effect is similar in shape at all beam momenta, but decreases in magnitude with momentum due to the $1/p$ dependence of multiple scattering. Estimated multiple scattering from our detectors and target systems are at about the 10 mr level at 153 MeV/c. A simple estimate is that the correction is on average 0.5% with an uncertainty of $1\%/\sqrt{12} = 0.3\%$, which we use in Table II. Multiple scattering corrections will be calculated for the data with simulations, and the final systematic uncertainty will depend on how well the simulations reproduce the data.

Two corrections that may not be evident arise from radiative corrections and from magnetic contributions to the cross section. Radiative corrections for the muon are estimated to be $< 3\%$, with overall uncertainties about one-tenth of the correction, or 0.3% and

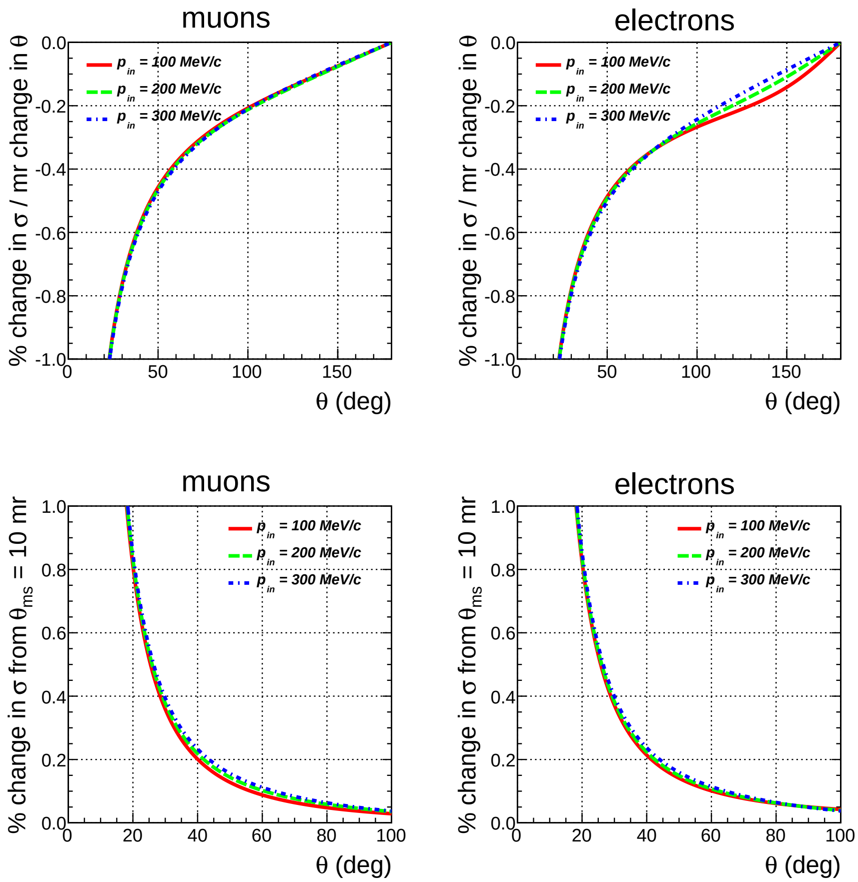

FIG. 8. Top: Change in cross section from a +1 mr offset in the scattering angle. Bottom: Change in the cross section from multiple scattering. Estimates were done with the Kelly form factor parameterization [20]. The multiple scattering calculation uses the simple Gaussian approximation.

angle-dependent variations smaller, about 0.1%. Electron radiative corrections and uncertainties are about 5 times larger. In the case of the muon, the radiative tail is quite small. For the electron, the radiative tail is long, so the correction includes averaging over a wider range of vertex kinematics from pre-radiation, and low-momentum outgoing electrons not triggering the detector.

For extracting the electric form factor and the charge radius, it is necessary to correct for magnetic contributions to the cross section, which grow as large as 30% at our largest beam momentum and scattering angle. The magnetic form factor is known to better than 1%, so the relative uncertainty from the magnetic correction is about 0.1% for the cross sections.

Finally, fits of pseudodata indicate that the normalization of the data sets to the $Q^2 = 0$ form factor can be done at about the 0.1% level for the form factor and the 0.2% level for the cross section. This is, however, an absolute normalization uncertainty that does not affect the relative cross sections within a data set.

These factors will be discussed in greater detail later, particularly in Section VIII C. Uncertainties related to event selection and background removal are discussed in Section VIII A.

III. THE πM1 BEAM LINE

A. Beam Line Parameters

The πM1 channel views the M1 production target at an angle of 22°. The channel includes focusing quads, two dipoles which each bend the beam 75° in the horizontal direction, and two sets of jaws. The default tune is point-to-point, producing an image of the production target at a path length distance of about 24 m. Figure 9 shows the beam distribution as measured in December 2013 with one GEM telescope and projected to the approximate location of the target. The beam width varies with momentum but is

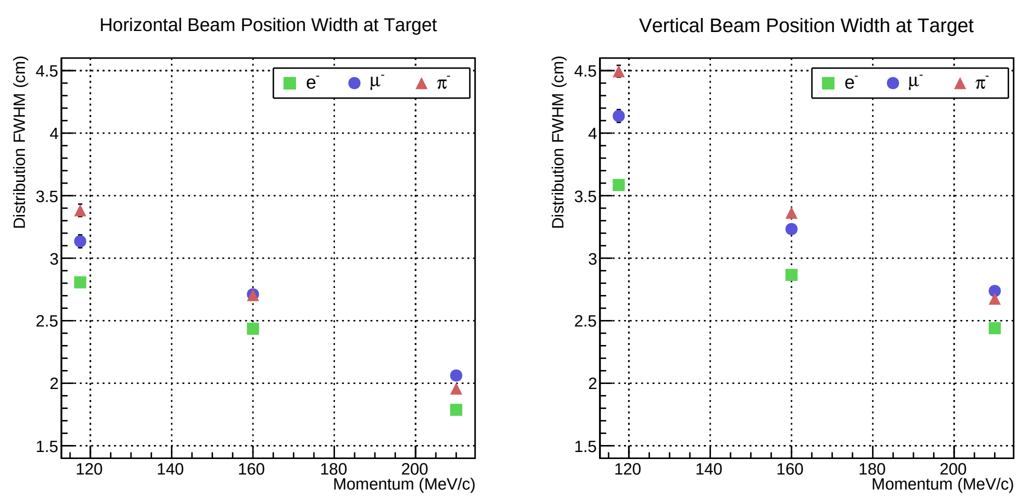

FIG. 9. FWHM of the beam as measured in the December 2013 test setup with GEM chambers as a function of momentum and particle type. The beam tune will be further optimized.

nearly independent of particle type. For the worst case the FWHM was 3.5 cm × 4.5 cm. The angular divergence of the beam was found to be at worst ∼45 mrad (FWHM) in the horizontal direction and ∼35 mrad (FWHM) in the vertical direction. We note here that the beam tune for this particular test run was not well optimized, and some of our studies have had better tunes with spot sizes at the target as good as 1 cm × 1.5 cm.

The πM1 channel fluxes were measured by Schumacher and Sennhauser in 1987 [22]. Fluxes for and properties of the μ's coming through the channel were not well established, but were measured in the MUSE 2012 and 2013 test runs. The RF spectrum was measured at several beam momenta, with resulting particle fractions for each polarity shown in Fig. 10. The results for the fluxes can be found in Table III; the numbers are based on the ratios measured in the MUSE test runs along with the absolute numbers from [22] scaled to a 2.2 mA primary proton current. No protons were observed in the channel with our detectors and our momenta settings.

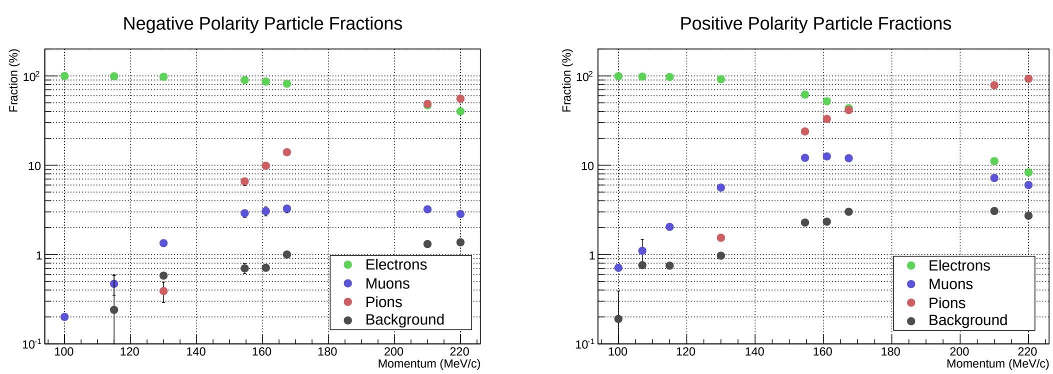

FIG. 10. Measured particle fractions versus beam momentum as measured in June 2013.

During the 2012 test run we also measured the beam distributions at the IFP, the background rates, and tested the dispersion. The standard beam tune has a horizontal dispersion at the intermediate focus point, at a distance of ≈12 m from the production target, of 7 cm/% and a resolution of 0.1%. TURTLE simulations predicted that the dispersed π beam at the IFP is 22.5 cm wide (full width at 10% maximum) with sharp edges, and the vertical beam distribution is roughly Gaussian with width $\sigma = 0.60$ cm, and no visible tails outside ±2.25 cm.

TABLE III. Beam flux at the target for full πM1 channel acceptance with 2.2 mA primary proton current. The total flux is based on previous measurements, while the relative fluxes of each particle types are based on MUSE test run measurements. Also shown in parentheses is the flux of each particle type when the combined flux is limited to 5 MHz.

Momentum (MeV/c)	Polarity	Total Flux (MHz)	e Flux (MHz)	μ Flux (MHz)	π Flux (MHz)
115	+	8.3	8.05 (4.85)	0.17 (0.10)	0.08 (0.05)
153	+	16.9	10.65 (3.15)	2.03 (0.60)	4.23 (1.25)
210	+	79.2	9.50 (0.60)	6.34 (0.40)	63.36 (4.0)
115	−	7.4	7.29 (4.93)	0.07 (0.05)	0.04 (0.03)
153	−	11.9	10.71 (4.50)	0.38 (0.16)	0.81 (0.34)
210	−	24.0	11.28 (2.35)	0.96 (0.20)	11.76 (2.45)

In our measurement, we found that all particles that reached the scattering target came through the IFP in a region about 20 cm wide by 5 cm high, with significant uncertainty in the horizontal direction, due to the SciFi detector used and its placement. We found about 0.1% of the beam was outside the 5 cm high beam region.

We checked the momentum dispersion of π's and μ's in the channel by using a collimator slot at the IFP and measuring the shift in the RF time resulting from the movement of the collimator. At 158 MeV/c, we found a dispersion of about 0.11%/cm, the same for π's and μ's, and consistent with the expected 0.14%/cm given the uncertainties from the tune used at the time and from the measurement itself.

The particle flux at the IFP was several times larger than the particle flux at the scattering target. Part of this difference is that 60% − 80% of the π's at the IFP decay before reaching the scattering target. A second part is the large flux of neutrons coming through the channel. This has led to a change in our baseline detector design at the IFP from a SciFi, sensitive to neutrons, to a beam Cerenkov, insensitive to neutrons.

B. Beam Line Detectors

The beam line detectors identify beam particle type (through RF timing and time of flight) for triggering from e's and μ's but not π's, separate muon scattering from muon decay in the target region (through time of flight), and measure the trajectory of particles into the target for determining the scattering angle.

For beam particle identification, particles are separated in RF time by 3 – 6 ns at the target region, and in flight time from the IFP to the target by 4.3 – 21 ns. More stringent concern is the 0.4 – 2 ns separation in time of flight of muon scattering events from muon decays in the target region.

The intrinsic angle variation of the beam, of ≈15 – 20 mr (σ), has a similar effect to multiple scattering, discussed in Sec II D, and is larger than our multiple scattering limit. The variation would lead to a large systematic correction and uncertainty if the incident trajectory were unmeasured.

1. Beam Cerenkovs

The beam Cerenkovs provide high-resolution timing of beam particles for RF time and time of flight (TOF) determinations, both between the IFP and the target region, and from the target to the scattered particle scintillators. The design is based on the work of Albrow *et al.* [23], who recently obtained timing resolution better than 10 ps with a beam Cerenkov, using quartz bars read out through a Photek PMT240 multichannel plate (MCP). The time resolution extrapolates to ≈50 ps with the lower energy πM1 beam and the thinner radiators that we plan to use; our design goal is to achieve 100 ps resolution. (We remind the reader of other related resolutions: beam particle intrinsic timing of 300 ps, scintillator resolutions of 30 – 50 ps, and beam SciFi resolution of perhaps 250 ps, if all planes fire, after corrections.) The beam Cerenkovs can be used in the trigger and in the analysis, but as noted in Section III B 2 they do not have the granularity to identify triggering vs. non-triggering tracks in the GEM chambers.

The baseline design with two beam Cerenkovs will be used, one at the intermediate focus and one at the target region. Sapphire Cerenkov bars will be read out with Photek PMT240 MCPs, the same PMT used by Albrow *et al.*. The PMT240 has a circular active area 4 cm in diameter, so multiple tubes read out multiple Cerenkov bars to cover the beam. The Cerenkovs will be tilted at the Cerenkov angle[2] from vertical relative to the

[2] The Cerenkov angle for $\beta = 1$ particles in sapphire (quartz) is about 56° (48°). For the muon beam momenta we propose, the Cerenkov light in sapphire (quartz) is emitted at about 42° – 52° (27° – 42°).

beam.

The IFP beam spot of about 5 cm high by 20 cm wide will be covered by 5 PMTs, alternately tilted upward and downward for high geometric efficiency. The required Cerenkov bars are then about 12 cm long. The target beam spot at the position of the Cerenkov, about 1 m upstream of the target and immediately before the SciFi, is roughly an 8 cm diameter circle. Thus there will be 4 PMTs for two offset pairs of radiators, one tilted up for the upper half of the beam and one tilted down for the lower half of the beam. This requires 11 cm long Cerenkov bars. This configuration gives good geometric efficiency while keeping the Cerenkov bars and the path length differences for particles shorter. The beam SciFi hit positions or GEM tracks will allow position corrections to be done for the target beam Cerenkov, but not for the IFP beam Cerenkov.

We have prototyped a beam Cerenkov detector, using both quartz and sapphire bars read out with a Hamamatsu R9779 phototube, the same tube we use for the scintillators. The Cerenkov bars were 3 mm $\times$ 3 mm $\times$ 8 cm long. As an example of results, with the prototype at the intermediate focus, we obtained 400 ps (σ) time-of-flight resolution between the IFP and target. This number includes contributions from path-length variations as well as the detector resolutions. Because the PMT240 has higher gain, faster response, and better quantum efficiency at short wave lengths than the R9779, we expect it to generate more photoelectrons and larger signals, and to provide improved timing. A PMT240 was obtained for tests to be conducted in 2014. A test of time resolution with cosmic rays passing through a sapphire Cerenkov bar read out with the PMT240 into a fast scintillator gave 140 ps (σ), not much larger than expected from purely geometric path length considerations.

2. SciFi Detectors

The beam SciFi provides a time measurement near the target that along with the RF signal determines the beam particle type. This timing signal is included in the trigger logic to identify muon- and electron-induced events and suppress pion-induced events. Here, the beam SciFi plays the same role as the beam Cerenkov, with greater rate capability due to its greater number of electronic channels, but with worse timing resolution.

In addition, the SciFi is used to identify the triggering trajectory if there are multiple tracks in the GEM chambers for a single event. The GEM chambers alone have an integration time of ≈100 ns, which sums over 5 beam RF buckets. With 5 MHz total flux this results in a second track in the GEMs for about 30% of events, and more than one additional track for about 10% of events. The beam SciFi has sub-ns resolution, and effectively hundreds of pixels, so that at the analysis level ambiguities should generally be resolvable. Same particle, same RF bucket background can be resolved if the scattered particle track clearly points to only one of the incident tracks.

The SciFi will be installed just upstream of the GEM telescope and immediately downstream of the target beam Cerenkov, about 0.9 m upstream from the target center for production data. The position is ≈22.6 m in flight path from the production target. To provide good efficiency, redundancy, and time and position resolution, the detector consists of 3 planes of 2 mm diameter circular fibers, arranged in a YUV configuration, with double-ended readout. The 3 planes will each have an active area of ≈ 8 cm $\times$ 8 cm with 40 fibers, leading to an octagonal area with acceptance for all 3 planes. To minimize the material in the beam all three planes will be in one light-tight box.

Tel Aviv University built a SciFi detector prototype in 2013 using Kuraray Photonics fibers of SCSF-81M ($n = 1.59$, $\rho = 1.05$ g/cm^3) material with polymethylmethacrylate (PMMA) ($n = 1.49$) and fluorinated polymer (FP) ($n = 1.42$) cladding, with total thickness 6% of the total fiber size. With 5.4% trapping efficiency, 2.2-m attenuation length, and 23% quantum efficiency, ≈15 photons per event per PMT are expected. Thus phototubes should have > 4 photo-electrons in 99.9% of events, and the efficiency of each plane should be close to the 94% geometric efficiency.

The prototype used a Hamamatsu 8804 maPMT, and obtained a time resolution of about 800 ps before and 600 ps after pulse-height corrections, for a single phototube. Due to double-ended readout, events with signals in all three planes have a time resolution a factor of $\sqrt{6}$ better, or about 250 ps. Efficient triggering – see Section V B – requires that we trigger on hits in 2 of 3 planes. The actual detector will be built with SCSF-78 fiber, which is expected to yield up to 30% more light. We note that the configuration of the fibers on the maPMTs at each end of a plane will be varied so that no two fibers are on adjacent pixels on both maPMTs, to reduce crosstalk.

3. GEM Chambers

Measuring high-precision cross sections requires knowledge of the scattering angle on an event-by-event basis at the level of several mr, but the divergence of the beam with the standard tune is 45 mr $\times$ 35 mr (FWHM) – see Section III A. Thus high-resolution tracking detectors are needed to measure trajectories into the target to reconstruct the scattering kinematics.

The most effective solution for tracking a $5-10$ MHz beam with $< 100\ \mu$m resolution is the use of GEM detectors (Gas Electron Multiplier). GEMs have been demonstrated to withstand harsh radiation environments while maintaining high resolution and efficiency for single events. Besides, they show little to no aging effects. GEMs have been successfully operated at intense high-energy muon beams at the COMPASS experiment at CERN, which has served as a role model for the development of GEMs in many other experiments and applications. They are low-mass detectors of order 0.5% of a radiation length, thus keeping multiple scattering at a minimum. Resolutions of $50-100\ \mu$m are typically achieved with a two-dimensional strip readout at some 400 μm pitch. This way the amplified charge is distributed over several readout strips as a few-mm wide cluster, which allows for an improved resolution smaller than the pitch by using a centroid weighting technique. The two-dimensional hit information from several GEM detectors is combined to determine the beam trajectory. The reduced number of electronics channels and a rather simple construction scheme makes GEM detectors very cost-effective.

The Hampton group developed, built, and successfully operated a set of 10×10 cm^2 GEM detectors at the OLYMPUS experiment at DESY [24], which aims to precisely measure the effect of two-photon exchange in elastic lepton-proton scattering at intermediate to high momentum transfer $Q^2 = 0.6 - 2.2\ (\mathrm{GeV}/c)^2$, by comparing the elastic electron and positron scattering cross sections. At OLYMPUS, these GEM detectors were used for monitoring of the luminosity by determining the forward-angle elastic *ep* scattering rate on an event-by-event basis. These GEM detectors became available for the proposed MUSE experiment at PSI in the course of 2013, after OLYMPUS data taking was completed.

Three GEM elements have been arranged as a tracking telescope with approximately 40 cm gaps in between GEMs. The GEM elements are identified as US (upstream), MI

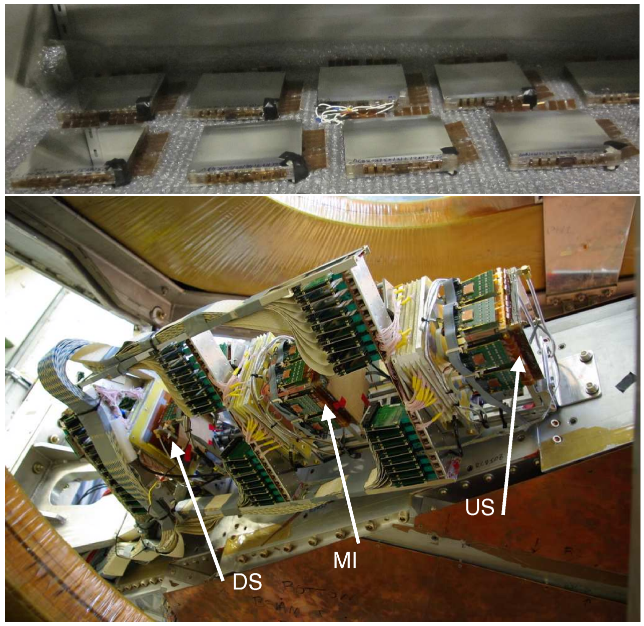

FIG. 11. Top: The final nine GEM elements produced for OLYMPUS. Bottom: Photo of the mounted tracking telescope for luminosity monitoring at OLYMPUS with the US, MI, and DS element labeled.

(middle), and DS (downstream), left and right sector. Figure 11 (upper half) is a picture of the nine GEM detectors produced for OLYMPUS. The lower half shows one of the GEM/MWPC tracking telescopes installed in OLYMPUS.

The 10×10 cm^2 OLYMPUS GEMs are operated with a 70% Ar / 30% CO_2 gas mixture and are read out with strips in two dimensions with a pitch of 400 μm. The design of the GEM stack parameters such as the drift gap and gaps between the three GEM layers and the readout plane follow that of the COMPASS design, which has been demonstrated to provide reliable detection of hit locations at routine rate densities of 2.5 MHz/cm^2 and of up to 25–100 MHz/cm^2 in dedicated tests. The expected rate density for the nominal πM1 tune at the final GEM just upstream of the target is about 5 MHz / 5 cm^2 = 1 MHz/cm^2, with a single-track probability of over 90%. Because the beam is coming to a focus the upstream GEMs will have a smaller rate density. The OLYMPUS GEMs are therefore very well suited to provide event-by-event beam particle tracking under these conditions.

The GEMs are read out using FPGA-controlled frontend electronics based on the APV-

25 chip developed for CMS. The readout hardware was developed by INFN Rome and Genova for the Hall A SBS spectrometer in the framework of the 12 GeV upgrade of Jefferson Lab, and was used for the first time in a realistic setting at OLYMPUS. It consists of a frontend card hosting the APV chip, which is directly attached to the GEM detector, and a VME based controller board hosting an FPGA located in the counting house at some 25 m distance. The APV processes 128 readout channels and pipelines both analog and digital information of 128 channels on a single cable. Raw signals on all strips are sampled with either 20 or 40 MHz frequency. After adjusting the latency, "snapshots" of the analog signal are taken and sent as frames to the VME based controller. The controller provides power, clock, and trigger to the APV, and receives and digitizes the raw data into on-board ADCs. The DAQ software is running on a CPU that controls the VME bus to write the data to disk or to send it to the event builder. As each APV chip reads out 128 channels, a 10×10 cm^2 chamber corresponds to 2x250 channels, which are read out with four frontend chips. One VME controller can operate up to 16 APVs, *i.e.* one such controller can operate up to four GEMs (two telescopes of three GEMs are in use, each read out with one separate controller). The strip numbers and digitized pulse heights of the hit clusters in x and y give the spatial information for the track. Figure 12 shows the digitized pulse height after pedestal subtraction of a single event versus the strip number, of the US, MI, and DS GEM in both x and y direction (250 channels each). The red triangles indicate the candidate cluster locations returned by the cluster finding algorithm.

The GEM telescopes at OLYMPUS worked very well. Operation was very stable, noise levels were very low. Intrinsic resolutions were found to be around 80 μm, and efficiencies around 95%, as shown in Figs. 13 and 14.

As mentioned above, this system became available for the MUSE experiment after completion of OLYMPUS in 2013, including expertise and manpower. Dr. Jürgen Diefenbach – who built and successfully brought the GEM system into operation when he was a post-doc at Hampton University – transferred the system from DESY and re-commissioned it at PSI in May 2013. The GEM readout was successfully added into the MUSE MIDAS DAQ and used in a further beam test in December 2013.

In the OLYMPUS experiment, the readout rate of the telescopes was ≈100 Hz. Within

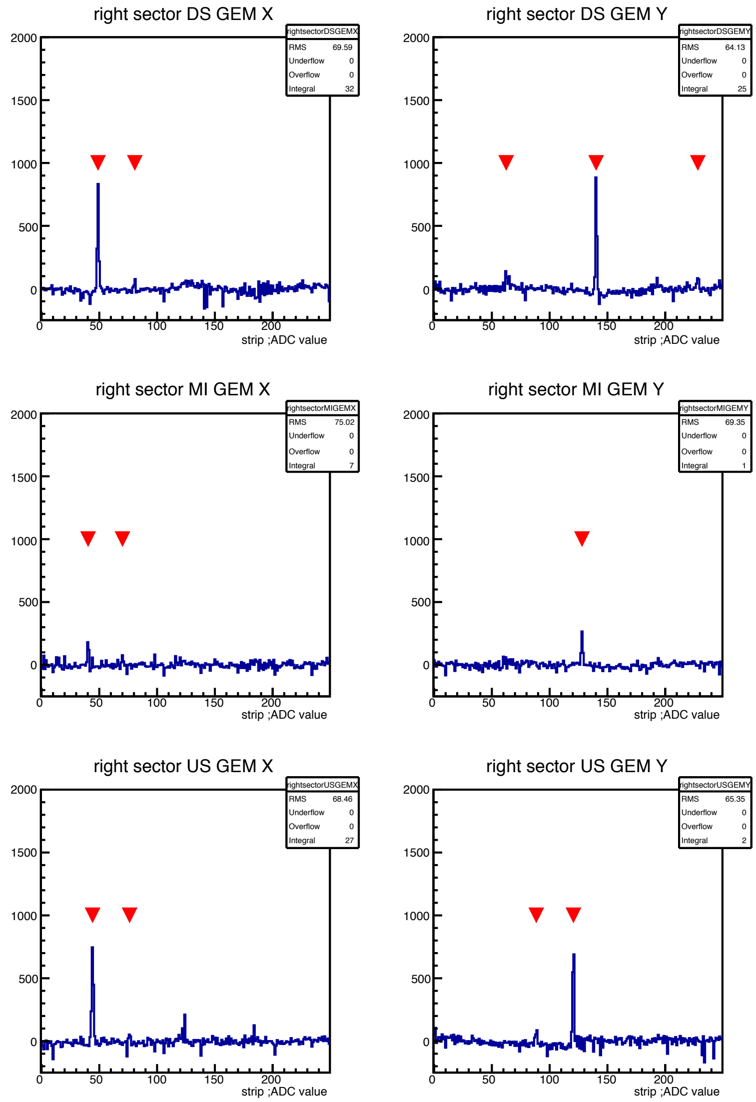

FIG. 12. ADC channel versus strip number in x and y direction for the US, MI, and DS GEM elements. The red triangles mark the location where the cluster finding algorithm yields a candidate cluster location.

the MUSE MIDAS system, both GEM telescopes were read out at a rate of ≈400 Hz. The MUSE experiment will use only a single GEM telescope, which should double the readout rate to ≈800 Hz. In order to achieve a readout rate of order 2 kHz, we plan to reduce the GEM event size. At present, each 32-bit word readout consists of 16 bits of data. Packing two 16-bit words into a 32-bit word should halve the event size and approximately double the readout rate. Also, the GEM readout can be sparsified (or zero-

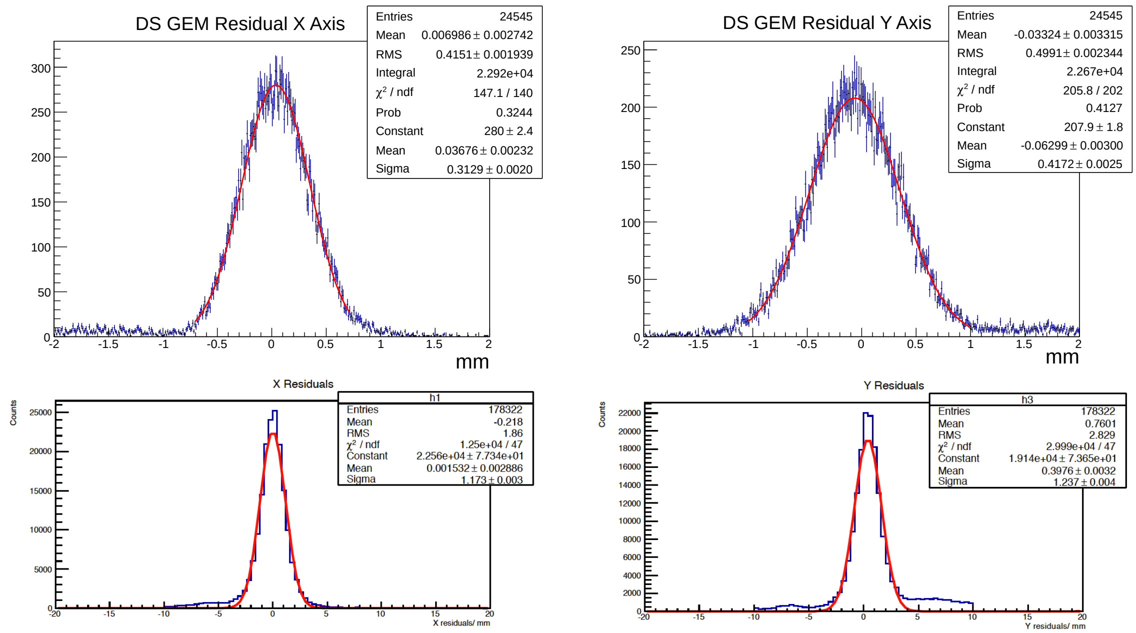

FIG. 13. Top: Track residuals for OLYMPUS forward-angle trajectories in the 12-degree GEM telescope fitted with 3 MWPC + 2 GEM elements. The residual width is composed of the intrinsic resolution and the track uncertainty. Intrinsic resolutions of around 80 μm have been achieved for the US, MI, and DS element, respectively. Bottom: Track residuals from the December 2013 test beam for MUSE beam trajectories in the GEM telescope fitted with 2 of 3 GEM elements. Residuals are bigger due to the less constrained tracks.

suppressed after pedestal subtraction), either at the hardware level or at the DAQ stage. Algorithms for sparsification in the presence of common-mode noise have been partially developed but not yet fully implemented. Noise levels in πM1 have not yet been studied, and it might be possible to reduce the noise levels and improve zero suppression.

4. Beam Line Scintillators

The beam line includes two sets of high-precision South Carolina scintillators – see Section IV B. There is an annular veto detector just upstream of the scattering chamber, and a beam monitor scintillator hodoscope about 1 m downstream of the target.

Concerns about the trigger rate from decay particles, from particles that scatter directly into the scintillators from the upstream beam line elements, and from particles in the beam

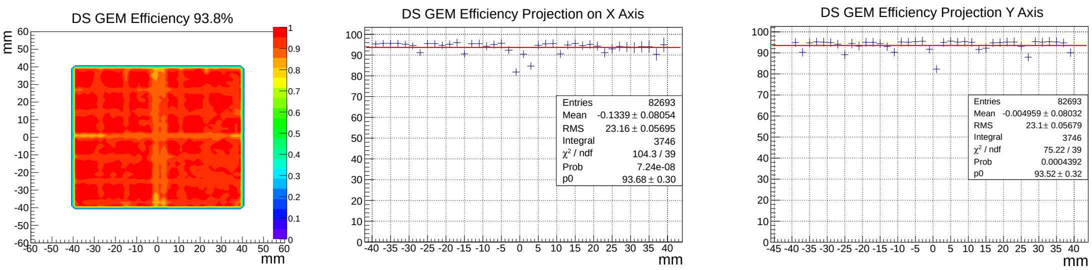

FIG. 14. Efficiency of the DS GEM element as a function of x and y. Tracks were identified and fitted with 3 MWPC + 2 GEM elements, in order to verify if the respective third GEM element shows a hit at the expected location. Some localized structures are visible related to weaker strips, which is under study. Efficiencies are generally around 95%.

tails interacting in the thick scattering chamber walls have led us to plan for an annular veto detector after the GEMs, at the entrance to the scattering chamber. The detector can be used to suppress readout of these types of events, as well as forward scattering from the upstream detectors. The veto is planned to have 8 segments each covering 45° of azimuthal angle, readout by 8 phototubes. Noise can be suppressed by high thresholds due to the large amount of light generated in the scintillors, but the segments will be optically coupled so that signals are seen in multiple phototubes. The geometry is intended to match the entrance port to the scattering chamber, and reduce the rate of singles trigger from the forward most spectrometer paddles.

Performing a high-precision experiment requires precisely monitored beam stability.[3] The πM1 beam line has limited instrumentation – slow controls give access to magnet currents and the primary proton beam current. An NMR probe will be installed to directly monitor the magnetic field of the downstream dipole magnet ASM12, but this alone will not guarantee beam stability. We will monitor beam stability and flux through the RF time spectrum of the beam.

The beam RF time is determined to high precision with the beam Cerenkov and SciFi signals for triggering events, which provide a biased sample, and at lower precision through random coincidences of other beam particles. The lower quality is due to using edge discriminators and not having pulse size information to improve timing of the random

[3] For completeness, we mention that the beam position and angle distributions will be monitored through background tracks in the GEM chambers – see Section III B 3 – and the beam flux will be monitored through the beam PID system – see Section V B.

coincidence tracks not in the same beam RF pulse.

Our beam tests with a high-precision scintillator in the beam line measured the momentum dispersion of the channel with 25 ps time shifts, monitoring shifts in π and μ peaks relative to the electron peak. The RF time measured with this precision provides 0.03% – 0.1% momentum stability measurements using either π's or μ's in our momentum range. To provide a continuous independent monitor of the beam stability at this level, we will install a high-precision beam monitor hodoscope about 1 meter downstream of the target. The hodoscope will consist of 6 scintillator paddles readout through constant fraction discriminators, as used in our beam tests, so that pulse-height corrections are not needed.

C. Target

Measuring elastic μp and ep cross sections requires scattering from a hydrogen target. We have chosen to use a liquid hydrogen target, rather than a solid CH_2 foil, to reduce the number of other nuclei in the beam, and thus to reduce the background subtraction. The George Washington University has assumed responsibility for the target.

Liquid hydrogen targets in vacuum systems are a mature technology, with existing targets capable of handling kW-level power depositions. For the experiment proposed here, the anticipated power deposition in the target is $P \approx 7$ MeV$\cdot$cm^2/g $\times$ 0.3 g/cm^2 $\times$ 10^7 e/s $\times$ 1.6×10^{-19} C/e = 3×10^{-6} W = 3 μW.

Recent examples of low-power, standalone, cryogenic target system are found at Fermilab[25], developed by the Michigan and Maryland groups, Jefferson Lab, developed internally, Mainz, Lund, built in house, and other facilities. These targets typically operate at a pressure slightly above atmospheric pressure, to limit infiltration of nitrogen, oxygen, or other gases that might freeze on the cryogenic target walls. We expect the LH_2 system for this experiment to be generally similar to these systems, but designed with our specific experimental parameters in mind.

In this section we will largely not consider issues of cryogenic target safety, instrumentation, *etc.*, since we are discussing these aspects with the local PSI groups. We expect a full safety review of the target will be required by the laboratory in the near future. We

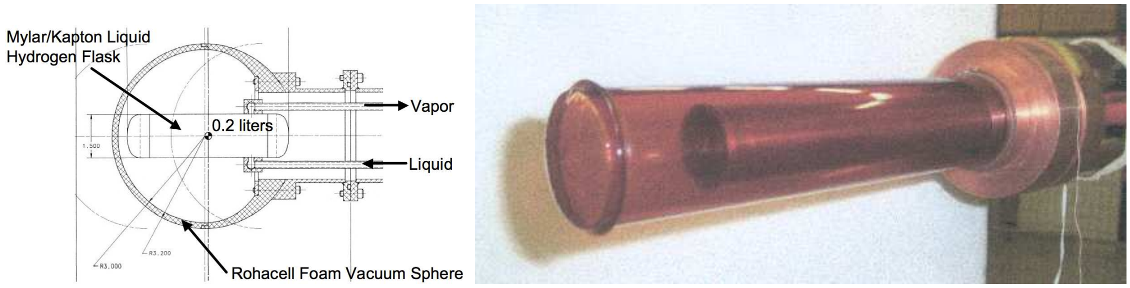

FIG. 15. Left: Drawing of the Fermilab E907 cryotarget. Beam enters from the right. Right: Picture of a kapton target cell used in Mainz MAMI A2 photon experiments. The entrance window and the tube on which it is mounted can be seen inside the kapton cell.

will instead focus of issues of the cryogenic cell design and vacuum system windows, since the interaction of the beam with these elements directly determines the statistics of the measurement, backgrounds, and resolutions, and on target systematics.

An example of a target system is the Fermilab E907 target [26], shown in Fig. 15. In this target the liquid hydrogen was contained in a 125 μm thick mylar/kapton flask. The vacuum system in the region of the target used an almost spherical shell 5 mm thick with a 15.2 cm inner diameter made of Rohacell (a low density foam) + fiberglass + epoxy. The target cell is made by gluing a sheet of mylar into a tube, and forming $\approx$2 cm long end caps that are then glued over the ends of the tube. Hydrogen liquid enters through the bottom and exits through the top of a support clamp that surrounds the tube, near the upstream end.

Figure 15 also shows an example of a kapton target cell used by the Mainz MAMI A2 collaboration for real photon experiments. Beam enters from the right. Hydrogen fills the region between the outer kapton cell and an inner aluminum tube which supports a kapton entrance window. The cell is formed by gluing a kapton sheet into a cylinder, and gluing on a short $\approx$5 mm long end cap. There is a small lip on the end cap to provide a larger gluing surface. Hydrogen enters and exits the cell through the metal base at the right edge of the photograph.

The standard Jefferson Lab high-power cryogenic targets use aluminum cells, typically with 0.1 mm thick walls, in a variety of geometries. The “beer can” geometry, shown in Fig. 16, is very similar to the Mainz kapton cell shown in Fig. 15, with the liquid hydrogen

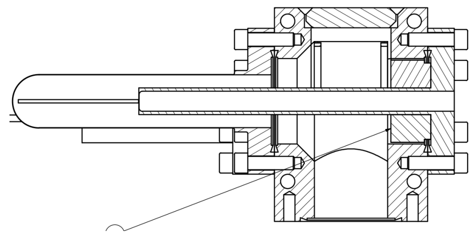

FIG. 16. Drawing (top view) through part of the Jefferson Lab Hall A cryotarget, showing the cell, flow diverter, and entrance tube and window to the left, and the cell block to the right.

pumped into one side of the cell, vertical flow diverters installed at the top and bottom of the cell cause the hydrogen flow to be largely transverse where the beam goes through the hydrogen, and the hydrogen flowing out the other side of the cell. The "tuna can", and "race track" configurations use a vertical flow configuration, with hydrogen entering the top of a thin walled cell and exiting the bottom.

For a low-power experiment such as ours, the slightly thicker 125 μm kapton flask is chosen. Kapton is preferred over mylar for hydrogen targets. It is superior to the thinner 100 μm aluminum in providing reduced multiple scattering ($\approx$0.044% of L_{rad} for kapton vs. $\approx$0.11% of L_{rad} for Al for entrance or exit window). Kapton also provides for a reduced energy loss (0.032 MeV for kapton vs. 0.044 MeV for aluminum for entrance or exit window) and lowers the rate of nuclear scattering backgrounds.

With the scattered particle detectors to the sides of the beam, constraints from a low-energy beam and multiple scattering, and a desired scattering angle range of $20^\circ - 100^\circ$, the optimal choice of the target cell configuration is similar to the Fermilab 907 design, but with a kapton cell with end caps of the Mainz design, and supports above and below, but not around the cell. Although the Mainz design has obvious lips that appear to have more material than the E907 flask, in the 907 design there is a $\approx$1 cm overlap of the cylinder and the end cap to provide a gluing surface, so there is actually more material in the 907 design. This configuration is shown in Fig. 17.

We are tentatively planning on a cell 4 cm long with a diameter of 4 cm. Based on the beam line measurements in Section III A, this will lead to only a small fraction of the beam tails going through the side walls of the cell. The cell size might be adjusted in light of the planned measurements of the beam size, but we note that whatever the cell size the

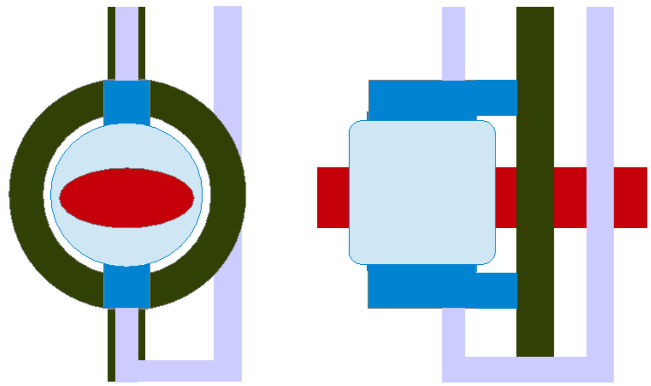

FIG. 17. Cartoon of the planned design for the target cell of this experiment: end view (left), side view (right). The beam passes through an annular support ring into the target cell. The cell is supported between two arms coming out from the support ring. Liquid hydrogen fill and vapor exhaust tubes attach to the kapton cell through the support arms. The cell is also wrapped in aluminized mylar (not shown).

beam halo will go through the walls, and fiducial cuts on the incoming particle will be a necessary part of the analysis.

The simplest way to construct the vacuum system is to mount the targets in a vertical vacuum pipe with a diameter of $\approx$15 cm. The cold head for the target will be at the top, but probably mounted separately connected by cryo lines to avoid coupling vibrations into the target system. The cryo lines will enter the top of the scattering chamber tube, above a bellows which will allow the target vertical position to be adjusted between cryocell, dummy foil, and empty target settings, while allowing all the electronics and motion system to be in air. The tube will require thin entrance and exit windows. The entrance window will be circular with $\approx$4 cm diameter, corresponding to an angular range of 31° in the backward direction. The exit window needs to be about 16 cm high and cover the angle range from -120° to +120°, so that the acceptance is not limited by scattered particles passing through the thick vacuum wall on their trajectory towards the scintillators. While the entrance window can be much thinner, about 50 μm of kapton, the exit window will need to be about 200 μm thick. Because the angle range of the windows is large, support posts might be necessary.

We are considering implementing a liquid nitrogen heat shield within the scattering chamber, for two reasons. The first reason is that any residual gas within the scattering chamber will tend to freeze to the LH_2 target, adding background to the measurement. The LN_2 heat shield will act as a cryopump, reducing the amount of residual gas that freezes to the target cell. The second reason is that the primary heat load to the target is radiation from room temperature vacuum system components. The LN_2 heat shield can reduce the heat load on the target by about a factor of two.

There are several contributions to the systematic uncertainty from the cryotarget:

- For operational temperatures about 19 K, the density change in the target is about 1.5%/K. With calibrated resistors the temperature can be determined to better than 0.1 K and thus the density to ≈0.1%.

- The variation of density with pressure is about 0.01%/psia. Pressure can be determined to at least 0.3 psia, so the uncertainty is small.

- Room temperature H_2 is largely in the ortho (spins parallel) configuration, but cryogenic H_2 liquid is >99.8% para (spins anti-parallel). The time constant for the conversion is of order a day for pure H_2, but typically small amounts of contaminants in the hydrogen shorten the conversion time significantly, an order of magnitude or more. The density difference between the two spin configurations is about 0.6%. As long as the cryotarget is cooled a few hours before data taking, the uncertainty from the ortho-para fractions is small.

- The equation of state is known to about 0.1% for LH_2.

- In high-power experiments, there is an issue of energy deposited in the target leading to boiling. For this experiment, the 3 μW expected from the beam is insignificant.

- Thermal radiation is, however, a significant issue. If we use $\epsilon = 1$, as for a black body, the room temperature surroundings radiate ≈3.5 W of power into the cryotarget cell, potentially leading to bubbles and density variations. This energy transfer is typically suppressed by wrapping the target in 8 or so layers of aluminized mylar, to reflect the thermal radiation. The emissivity of aluminized mylar or kapton is ≈0.03.

- The length of the target cell varies with temperature. It is possible to estimate the change in length form thermal expansion coefficients, and to measure the change in dedicated tests. This uncertainty is typically a few tenths of a percent.

- The target cell length for the planned design varies by about 5% from the center to the edges. It will be necessary to measure the beam position and angle distributions and use a Monte Carlo to determine the average thickness. Since the central 2σ of the beam are about 2 cm diameter, versus the 4 cm cell, the total variation in length for much of the beam is only about 2%. The uncertainties will have to be evaluated from the simulation, but are likely not more than a few tenths of a percent.

- The position of the target has to be determined relative to the beam. Spectra of reconstructed z_{target} from particles scattered at large angles can likely determine the z position of the target to $\approx$0.5 mm, but the data cannot be used to determine the transverse positions. The uncertainty typically leads to several tenths of a percent uncertainties in systems with relatively larger curvature of the end caps compared to the beam size. Here it appears to be smaller.

Considering the above points, it appears that the point-to-point systematic uncertainty due to the cryotarget is negligibly small. There are small angle-dependent corrections as the amount of material particles pass through is different at different angles. For each beam momentum the target contribution to the luminosity is the same for all points. When beam momenta are changed, the energy deposited by the beam in the target is so small that the momentum change does not matter. The likely issues with the point-to-point uncertainty, which will need to be evaluated based on the target performance during the run, are whether there are any day-night or seasonal changes in ambient temperature that lead to differences in thermal radiation and boiling in the target, and whether the target operates stably. Power glitches or reboots of electronics could affect the target density.

For the absolute density, there are several effects that are at the 0.1% level, and the total uncertainty should be about 0.5%. Achieving this uncertainty in practice will require dedicated measurements to understand what, if any, target boiling there is from thermal radiation, and how the target cell length and position vary when the target is cooled. Dedicated measurements can be done either optically or with X-rays.

IV. SCATTERED PARTICLE SPECTROMETER

A. Straw Chambers

The chambers must provide, neglecting multiple scattering, position resolutions of about 150 μm and angle resolutions of about 1 mr, and be aligned to determine the absolute scattering angle to better than 1 mr. They must be able to operate at singles rates of a few hundred kHz, and efficiently detect and track particles that are close to minimum ionizing. The MUSE experiment will make use of recent developments in Straw Chamber design [27] which are also being implemented for the PANDA experiment [28]. These chambers allow for significantly less straw material by over pressuring the straws to provide mechanical stability.

The construction of the straw chambers will be the led by the Hebrew University group, which has extensive experience is electronics, gas, and vacuum systems design. Dedicated space for the construction has already been assigned at the Hebrew University.

The PANDA design has been shown [27] to operate successfully at rates exceeding 8 kHz/cm, significantly higher than the expected rate for the MUSE experiment, and have achieved a position resolution of $\approx$150 μm. The straw chamber will consist of 2 chambers on each side of the detector, each with 5 Y planes and 5 X planes, for a total of 10 straw planes. In order to provide better resolution on the scattering angle, the vertical straw planes will be placed closer to the target.

The chambers will be constructed by gluing the individual straws together using a precision machined jig. Straw positions will be confirmed using a well collimated radioactive source, matched to a camera and position controlled by a precision stepper motor. In addition, the same camera setup will be used to accurately determine the position of the crimp pins used to hold the wires. With this setup we expect to be able to determine the pins positions to better then 10 μm using a high-resolution CCD camera. Since we require the resolution to be on the order of 150 μm, the expected wire sag should be significantly less than that. The gravitational sag of a horizontal wire can be calculated via:

$$\delta = \frac{ML}{8T}, \tag{2}$$

where M and T are the wire mass and tension in grams, and L is the wire length. For our configuration the maximal sag is less than 15 μm. Further, the horizontal wires which sag from gravity measure mainly the azimuthal angle, while the vertical wires which do not sag gravitationally measure mainly the scattering angle.

The electric field acting on the displaced wire induces an additional shift on the wire which is maximally

$$h = \frac{L^2 V^2 (4\pi\epsilon)\delta}{9.8 \times 16 T R^2 \left[\cosh^{-1}(R/2r)\right]^2}, \tag{3}$$

where L is the wire length, T is the tension, R is the tube radius, r is the wire radius, V is the applied voltage, and δ is the deflection. For a 15 μm deflection we obtain an additional sag of 0.7 μm. Even for an extremely conservative scenario of 50 μm sag, we obtain an additional deflection of 2.2 μm. We therefore conclude that wire sag due to either gravitational sag or electrostatic deflection will have a negligible effect on the achievable resolution.

The chambers will be operated using a mixture of 90% Ar/10% CO_2, with the straws held at a pressure of 2 bar using pressure control transducers and mass flow controllers (Bronkhorst Ltd.). Each of the 4 chambers will be provided with an independent gas supply system. The gas mixture will run in continuous flow mode, completely replacing the full gas load in the chambers every 12 hours, which will allow us to run without bubblers. The straws will be run at 1700V and will be read out by a specially constructed version of the PADIWA3 frontend card (see Section V A) read out in turn by TRB3 TDCs. The PADIWA boards accept analog input, are internally impedance matched, and output LVDS signals to the TRB3, a configuration which will allow us to forego level translators.

Straw spacing is 1.01 cm, and adjacent offset straw planes are centered 0.87 cm apart. High tracking efficiency requires 5 planes of straws in each direction, which will be 4.5 cm thick. X and Y planes combined will be about 9 cm thick. The first straw chamber in each spectrometer will be centered about 30 cm from the target with a size about 60 cm x 55 cm, and the second will be centered about 45 cm from the target with a size about 90 cm x 80 cm. No stereo planes are needed. The low beam flux reduces the likelihood of multiple interacting beam particles, and most secondaries are forward-going delta or Moller electrons. The rear scintillators provide a crude 2d position which should generally allow extraction of multiple tracks in the rare cases when they occur. These assumptions lead to 2 rear chambers each with 400 90-cm long vertical straws and 450 80-cm long horizontal straws, and 2 front chambers each with 275 60-cm long vertical straws and 300 55-cm long horizontal straws. The total number of straws in the system is 2850.

The location of the chambers from the pivot and their sizes are summarized in Table IV along with the number of straws per chamber. The spacing between the chambers will be about 6 cm from the back of one chamber to the front of the next chamber. Assuming a resolution of 150 μm and having the center of the front and back chambers spread out over a 15 cm distance will provide about a 1 mr angle determination. The determination is improved by having more than the minimal four planes needed to resolve left-right ambiguities, but ultimately limited on an event-by-event basis by multiple scattering.

TABLE IV. Straw chamber parameters including the distance from the pivot, chamber active area, and the number of straws.

Chamber	Distance (cm)	Active Area (cm^2)	Number of Straws per Chamber
Front	30	60×55	575
Back	45	90×80	850

The determination of the relative positions of the chambers and the scattering angle with our plan to use the GEM chambers will be discussed in Section VII.

B. Scattered-Particle Scintillators

The scattered-particle scintillators are part of the event trigger and help with the particle separation via time-of-flight (TOF) measurements. This requires high detection efficiency for the particles of interest and excellent timing resolution.

The Experimental Nuclear Physics Group at USC is committed to build the scattered-particle scintillators for the MUSE experiment. The group has extensive experience in assembling large time-of-flight detectors. It has also designed and prototyped the new FToF12 detector for the upgraded CLAS12 at Jefferson Lab. All scintillators have been built, fully assembled, and tested at USC. They are now installed in the forward carriage of the new CLAS12 detector. With only the exception of the thickness of the scintillator bars, we are planning to copy the design and construction procedures of the FToF12 bars. The FToF12 scintillation bars are rectangular in shape with a cross sectional area of 6 cm $\times$ 6 cm. Position-dependent time resolutions have been measured in cosmic tests for scintillator bars of various lengths; see Fig. 18. Average time resolutions of $\sigma_{avg} = 34$ ps and $\sigma_{avg} = 51$ ps for the 69 cm long and 203 cm long bars, respectively, were achieved.

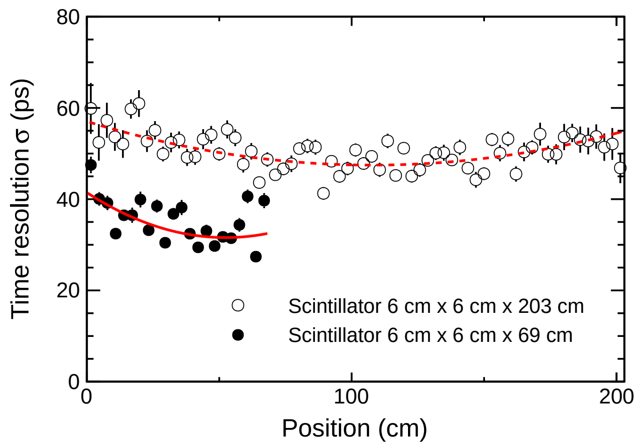

FIG. 18. Position-dependent time resolution for two CLAS12 203-cm and 69-cm long scintillator bars after calibration, event selection, and time-walk correction. The average time resolution is $\sigma_{avg} = 51$ ps for the 203-cm bar and $\sigma_{avg} = 34$ ps for the 69-cm bar, respectively [29].

The detector will be made of Saint-Gobain BC-404 plastic scintillators, which have a high light output and fast rise time. Each end of the scintillator is fitted with black tape, which masks the corners while leaving a circular window that extends one millimeter into the area that will be covered by the photocathode. The corner blocking reduces the amount of reflected light contributing to the leading edge of the PMT signal. Hamamatsu R9779 PMTs are then glued to each end of the scintillator. The bare counter is wrapped with precision-cut aluminized mylar and DuPont™Tedlar. The Tedlar film extends beyond each PMT onto the anode, dynode, and high-voltage cables, providing a single light-tight casing for the entire counter. Details about the construction process and system tests for quality assurance can be found in Ref. [29]. Table V lists the design parameters for the scintillator walls. The front wall is square and covers at least a horizontal angular range from 20° to 100° from all points within the target. The back wall is also square with an increased angular acceptance to account for particles which scatter in the front wall material.

TABLE V. Design parameters for the scintillator walls.

	Front wall	Back wall
Number of scintillator bars	17	27
Scintillator cross section	6 cm × 2 cm	6 cm × 6 cm
Scintillator length	112 cm	211 cm
Target to front-face distance	50 cm	73 cm
Gap between scintillator bars	0.02 cm	0.02 cm
Scintillation material	BC–404	BC–404
Photomultiplier	Hamamatsu R9779	Hamamatsu R9779

We have studied the performance of the proposed scattered-particle scintillators with Geant4 simulations of the planned setup. The particle interactions and their energy deposition within the scintillators have been calculated. Figure 19 shows the distribution of deposited energy in a 5 cm × 5 cm scintillator which was used in the summer 2013 test measurement at πM1. The incident particles were 153 MeV/c muons. The simulated energy distribution agrees nicely with the measured data. The energy deposited by particles whose paths do not traverse at least the full thickness of the scintillator is lower than the energy of the lower edge of the Landau-like portion of the energy distribution.

Simulated energy distributions for the 6 cm × 2 cm and 6 cm × 6 cm scintillator bars are shown in Fig. 20 for scattered electrons (left panel) and muons (right panel) at various beam momenta. The set of curves with low energy deposition is for the front wall; the set of curves with high energy deposition is for the thicker back wall. In the studied range, the energy depositions for $e^{\pm}$ are independent of the beam momentum. The simulation shows for each event the maximum energy deposition in any front- or back-wall bar. Very nearly all events have energy depositions above threshold, $E_{th} = 2$ MeV, in (at least) one bar. The detection efficiency is indeed very high.

A detailed view of the particle detection efficiencies for the scattered-particle scintillator walls at 115 MeV/c is shown in Fig. 21 as a function of the particle scattering angle. All

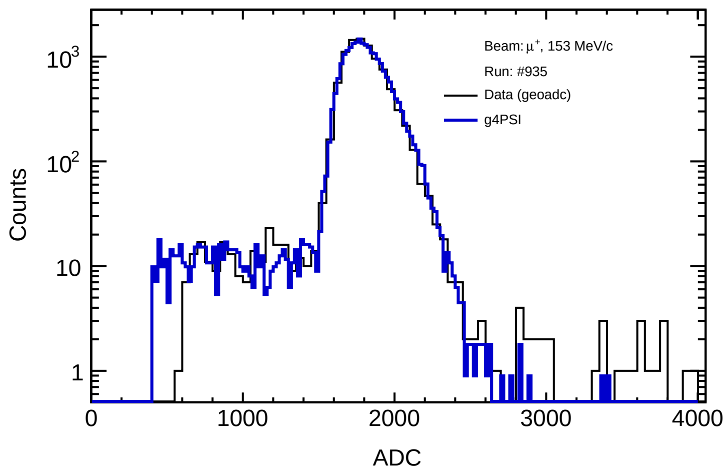

FIG. 19. Deposited energy of muons passing through a 5 cm $\times$ 5 cm scintillator bar. The data are from the summer 2013 test measurement at $\pi M1$. The blue histogram shows the result of the Geant4 simulation.

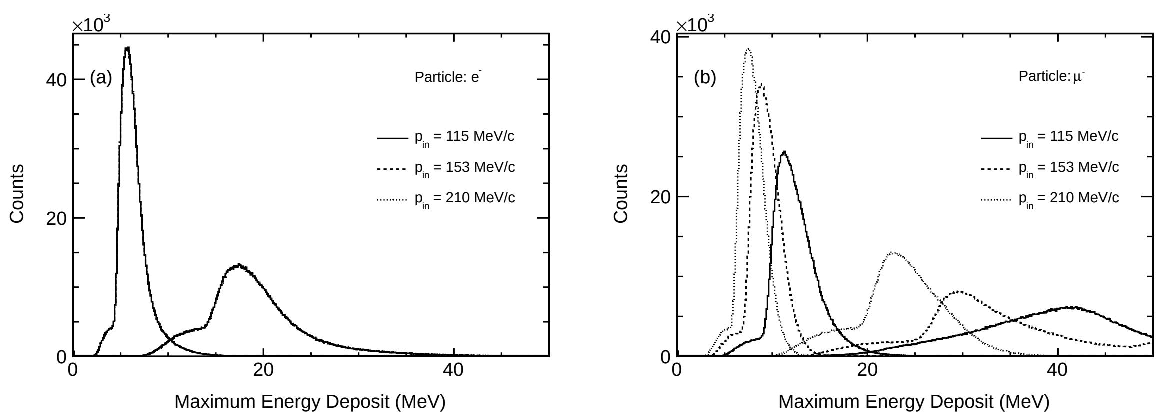

FIG. 20. Simulated energy deposition for scattered electrons (left) and muons (right), traversing the 6 cm $\times$ 2 cm bars of the front and 6 cm $\times$ 6 cm bars of the back scattered-particle scintillator wall. The simulation recorded for each event the maximum energy deposition in a scintillator of a given plane.

panels are for the same detection threshold of $E_{th} = 2$ MeV. The solid dots give the ratio of events with an above-threshold hit in the front plane per incident particle. Particles were incident on the "active" area of the scintillator plane; the physical size of the plane is slightly larger. The overall geometrical acceptance for the "active" area is shown in Fig. 22.

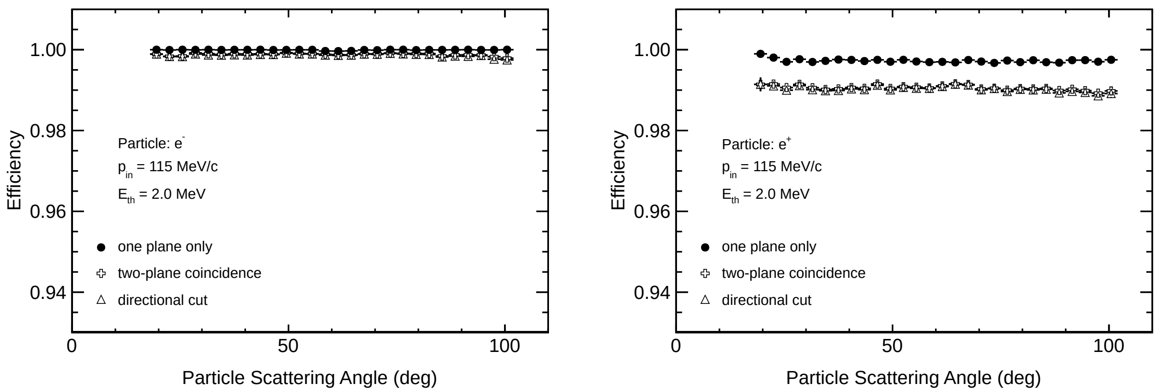

FIG. 21. Estimated detection efficiency as a function of particle scattering angle for e^+ and e^- at beam momenta of 115 MeV/c. The change of momentum of the scattered particle with scattering angle is taken into account.

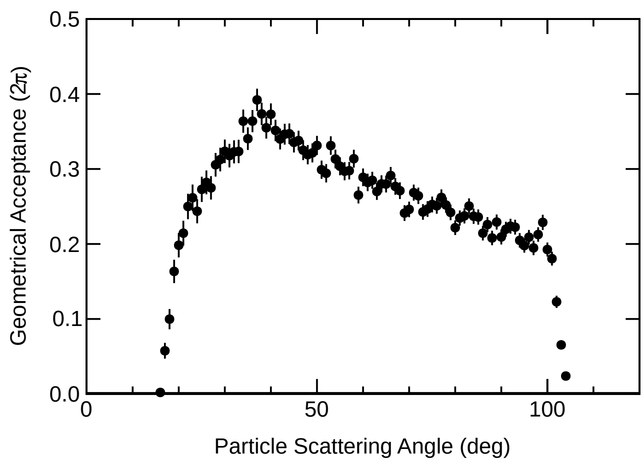

FIG. 22. Estimate of the geometrical acceptance of one scintillator wall as the fraction of high-energy muons originating from the target and uniformly distribution which hit the wall.

This one-plane efficiency is practically 100%. The two-plane coincidence (plus symbol in Fig. 21) requires above-threshold hits in both the front and back planes. It is in all cases well above 99.5%, except for e^+. The "directional cut" (triangle points in Fig. 21) utilizes the fact that scattered particles, which originate in the target, deposit energy mostly in certain combinations of front- and back-wall scintillators. For an event to pass this cut, each hit in a scintillator bar of the back wall must coincide with hits in up to three corresponding neighboring scintillators in the front wall. This directional cut does not affect the efficiency much but helps to suppress triggers from background events which do not originate within the target. Figure 23 illustrates this correlation of scintillator-bar numbers for muons with different momenta originating in the target volume.

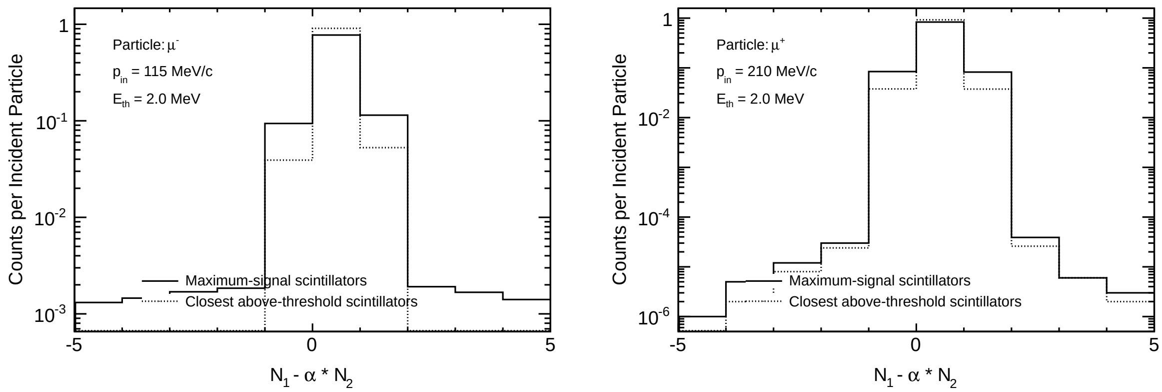

FIG. 23. Typical paddle-number correlations between paddle numbers N_1 and N_2 from the front- and back-wall scintillators, respectively. The factor α is the ratio of the distances from to the target to the scintillator-wall mid-planes.

Table VI summarizes the result of our efficiency estimates. While the μ detection efficiency remains well above 99% for all momenta, the e efficiency starts to decrease at thresholds larger than 2 MeV.

Figure 24 shows a simulation of the reconstructed reaction vertex for e^- along the beam line, $x = y = 0$, where the reconstruction only uses the position of hit bars and their geometrical position in the lab. Events shown have above-threshold hits in the front and back scintillators walls and fulfill an additional directional cut. The figure shows the effectiveness of the directional cut. The distribution for a μ beam is similar.

We have estimated background rates in the scattered-particle detectors. Beam particles, $\pi^\pm$, $\mu^\pm$, and $e^\pm$, at a rate of 1 MHz with momenta of 115, 153, and 210 MeV/c, respectively, were sent in the $+z$ direction and allowed to decay, to scatter off air, or off the target. The resulting raw rates in one set of the scattered-particle detector planes are summarized in Table VII and do not include trigger-level or offline analysis cuts other than the detection threshold and scintillator-bar coincidence requirement as indicated. The background rate from pion beam particles is dominated by their decay products and can be separated from the events of interest by RF time and time-of-flight measurements. The background events

TABLE VI. Expected average detection efficiency for scattered particles detected in coincidence between the front and back scintillator walls and requiring a three-bar directional cut.

Particle	Beam Momentum	Coincidence efficiency for various signal thresholds			
	(MeV/c)	0 MeV	1 MeV	2 MeV	3 MeV
e^+	115	0.9944	0.9918	0.9902	0.9833
	153	0.9955	0.9934	0.9920	0.9852
	210	0.9964	0.9948	0.9939	0.9874
e^-	115	0.9992	0.9989	0.9987	0.9929
	153	0.9994	0.9992	0.9990	0.9933
	210	0.9996	0.9994	0.9993	0.9937
μ^+	115	0.9991	0.9990	0.9989	0.9989
	153	0.9996	0.9995	0.9995	0.9994
	210	0.9997	0.9997	0.9997	0.9995
μ^-	115	0.9991	0.9990	0.9990	0.9989
	153	0.9995	0.9995	0.9994	0.9994
	210	0.9997	0.9997	0.9997	0.9995

can be largely suppressed on the analysis level also. As all of these particles are of low momentum, the background can be further reduced by a cut on the energy deposition in the second, thick, scintillator plane. Figure 20 shows that practically all electrons from the events of interest deposit at least 7 MeV in that plane; requiring a signal of at least 6 MeV reduces the coincidence rate by about an order of magnitude.

One background that we are continuing to study at this point in time is low-energy (10 – 20 MeV) electron recoils at forward angles, $<25°$, that might generate triggers. The rate of these is not large, but they have to be rejected at the analysis level. Most, but not all, of these events reconstruct to positions upstream of the target. Because of the large statistical variations in the energy deposited in materials – see Fig. 20 – additional information that allows these events to be rejected is desirable. These events appear to typically have a forward going "high" momentum beam particle that continues into the

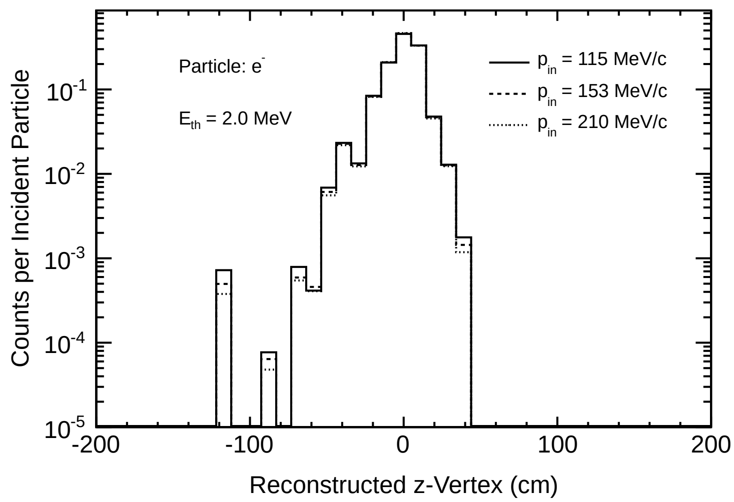

FIG. 24. Simulation of the reconstructed reaction vertex along the beam line, $x = y = 0$, using only the scintillator bars for scattered e^-. The distributions are similar for positively charged leptons. Included are all front- and back-wall scintillator paddles with a signal larger than the threshold.

high-precision beam scintillators after the target, which might by itself be sufficient to remove these events from the analysis. We are also considering a partial third scintillator plane for the most forward part of the acceptance, as these low-energy recoils will be ranged out before the third plane.

If uncorrected, detection inefficiencies in the scattered-particle detector will lead to errors in the measured cross sections. The average corrections for detector inefficiencies are on the order of 0.1% for $\mu^\pm$ and e^- and is on the order of 0.4% to 0.9% for e^+; see Table VI. These values require a threshold of $E_{th} = 2$ MeV. The positron efficiency is reduced due to possible annihilation processes. The detector inefficiencies show some angular dependence at low scattered particle momentum (backward angles at 115 MeV/c beam momentum); see Fig. 21. After correction for these effects, we expect the contribution from the scattered-particle detector to the systematic uncertainties of the absolute cross section to be less than 0.1%. The uncertainty is larger for $e^\pm$ cross sections if the threshold can not be kept stable. Because of their very similar detector response, we expect the contributions to the systematic uncertainties of relative cross sections for μ^+ and μ^- to be negligible. Also, the $\mu^\pm$ and e^- relative cross section uncertainties should be much smaller than 0.1%.

TABLE VII. Expected rate in *one* set of scintillator walls from beam-particle target-scattering and decay in flight from $z = -1.5$ m before the target to 5 m after the target. Values are given in above-threshold scintillator rate *per 1 MHz beam-particle rate* with a threshold energy of $E_{th} = 2$ MeV. The coincidence rate includes a three-bar directional cut. The coincidence rate not vetoed removes those events that deposit energy above threshold in the veto detector between the last GEM chamber and the scattering chamber.

Particle	Momentum	Front Wall (Hz)		Back Wall (Hz)		Coincidences	Coincidences Not Vetoed
	(MeV/c)	1^{st} bar	any bar	1^{st} bar	any bar	(Hz)	(Hz)
π^+	115	13844	67002	12904	61508	32779	18492
	153	9982	36599	11039	33679	22878	11438
	210	6163	15934	7272	12483	10045	4225
π^-	115	13830	66604	12719	60568	32128	17926
	153	10044	36864	10893	33780	23130	11562
	210	6090	15666	7290	12281	9986	4157
μ^+	115	618	1589	517	1684	1032	287
	153	167	686	186	833	446	201
	210	158	999	139	673	267	139
μ^-	115	582	1604	516	1755	1070	292
	153	147	631	161	745	385	190
	210	173	1012	165	697	261	140
e^+	115	1575	10341	868	3958	1547	306
	153	1467	9812	720	3621	1216	369
	210	1467	10006	715	3627	1209	529
e^-	115	1818	11603	1004	4452	1854	361
	153	1564	10868	835	4046	1517	412
	210	1638	10809	847	3928	1418	585

V. TRIGGER

A. Trigger Overview

The goal of the trigger system is to efficiently identify and read out scattered e's and μ's, while suppressing backgrounds, in particular the large rate of π-induced events. The primary trigger requires a beam PID system that identifies a beam e or μ, and a scattered particle system that identifies a "high-energy" scattered particle.

The beam PID is accomplished through timing measurements in the beam Cerenkov (Section III B 1) and SciFi (Section III B 2). The signals are processed in an FPGA to identify e's and μ's to accept and π's to reject, as will be discussed in Section V B. Due to the number of detector channels, the beam SciFi will be processed in one FPGA, while the beam Cerenkovs will be processed in a second FPGA, along with signals from the beam veto and monitor detector (Section III B 4).

The scattered-particle system uses scintillator signals, processed in an FPGA to determine the coincidences. Section IV B describes thresholds, efficiencies, and how well the paddles point to the target. For the primary trigger, we plan to require coincidences in both PMTs of two paddles to suppress noise.

A final FPGA will take the beam PID and scattered particle FPGA signals and perform logic to decide on whether to trigger.

There are a number of hardware systems that can be used to implement the FPGA logic. Our previous experience is with custom FPGA systems developed at Rutgers University by Ed Bartz of the Department of Physics & Astronomy electronics shop, and with CAEN v1495 systems, which we helped design and implement for the Fermilab E906 trigger. Here we plan to make use of the capabilities of the TRB3 system – see Section VI A – to use the FPGA in the TRB3 to perform logic on the detector signals. We plan to use 5 TRB3s in the trigger system, four for the beam Cerenkovs and scintillators, SciFi, left spectrometer, and right spectrometer, and one to take the outputs of these FPGAs and act as the Trigger Master.

Several secondary triggers are planned to be prescaled and read out. Examples include scattered pion, beam particle and random / pulser triggers, for a measure of backgrounds and how they might contaminate the data, and loose scattered lepton triggers, for trigger efficiency studies. The entire system will also be studied by varying beam flux from a low flux with few accidental coincidences up to the operating beam flux. The exact trigger conditions (timing offsets, coincidence widths, *etc.*) will need to be optimized under experimental conditions.

For isolated and well identified beam particles, triggering decisions are straightforward, but handling scattered-particle events when there are multiple beam particles is more difficult. Typically we expect to generate a trigger if there are two beam leptons, but not if one or both of the beam particles is a pion.

B. Beam PID System

The beam particle identification (PID) system identifies beam particle types to efficiently trigger on lepton scattering events and suppress π-induced events. At minimum, the beam PID system consists of the following:

- the target SciFi array, with 3 planes of 40 fibers, each read out at both ends with Hamamatsu maPMTs, for a total of 240 signals,
- the RF time signal from the accelerator,
- and FPGAs which process the signals from the detectors and accelerator to determine beam particle type.

Here we show that this minimal system is sufficient to identify particles with high efficiency. In practice, the signals from the IFP and target beam Cerenkovs will also be added to the beam PID system to further improve differentiation between particle types through time of flight.

As an example of how the beam PID system may work, we consider a programming scheme in which the beam RF acts as an FPGA clock, and particle RF timing is determined to be within one of 16 $\approx$1.25-ns wide bins. Because the FPGA is reprogrammable, the conditions for identifying particles – the RF time window for each particle type, the time of flight, the necessary number of planes[4] for each particle type to be considered identified, and the combination of such conditions – can be adjusted for each beam momentum setting to optimize trigger performance. This is needed as the relative timing of particles and the severity of the pion background vary with momentum.

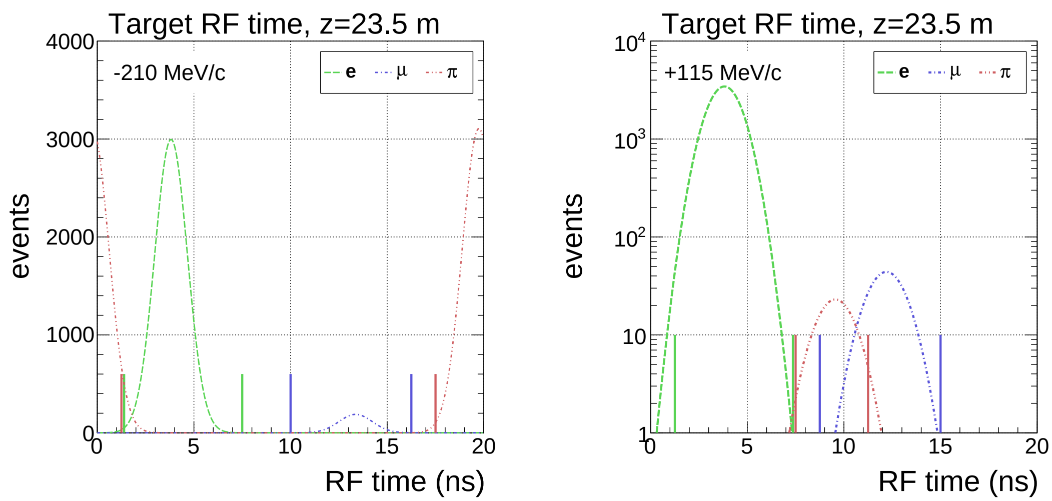

FIG. 25. RF time distributions at the target for -210 MeV/c (left) and $+115$ MeV/c (right) beam momentum. The distributions are for a single PMT signal before pulse-height corrections are made. The short vertical lines indicate the cuts used to identify particle types, as described in the text. The separation between particles is best at 210 MeV/c, and worst at 115 MeV/c.

The ability of the system to identify beam particle types is demonstrated in Fig. 25, which was generated based on the expected fluxes of e, μ and π, the reduced channel momentum acceptance, and a 0.8 ns (σ) resolution of a phototube added in quadrature to the as-measured intrinsic peak width. Here we only consider the main peaks, since backgrounds are small and will be eliminated at the analysis level. To investigate the efficiency of the 16-bin timing scheme, we used a simple algorithm with the target SciFi array data. The centroid of the RF peak determined the central bin of the timing window. The best configuration used a 5-bin window (a 6.25 ns wide region) for the identification of electrons and muons, and a 3-bin window (a 3.75 ns wide region) for identification of pions.

To calculate the efficiency, signals were simulated for six "phototubes" or hits (one for each end of each plane). The signals were compared with the assigned particle bins to

[4] Since the SciFi planes have a 94% geometrical efficiency, a requirement that all three SciFi planes have signals would lead to a trigger efficiency of 83%. A requirement of at least two out of three gives 99.0% efficiency.

identify an e, μ, π (an event can be identified as two types – *e.g.* μ and π). To identify an event as a π-induced event, 3/6 tubes must ID a pion. To identify an e- or μ-induced event, we require 4/6 tubes to ID the event correctly. The resulting efficiencies using this algorithm are shown in Table VIII. These results are independent of beam polarity.

TABLE VIII. Probability of identifying a particle as a given type from RF times measured by the three SciFi planes. Geometric efficiency and cut efficiency with a simple algorithm are included. See text for details.

Momentum (MeV/c)	Detector	Particle Type	Fraction e ID	Fraction μID	Fraction π ID
115	Target SciFi	e	0.9920	0.0000	0.0000
115	Target SciFi	μ	0.0000	0.9714	0.0198
115	Target SciFi	π	0.0000	0.0000	0.9918
153	Target SciFi	e	0.9920	0.0105	0.0000
153	Target SciFi	μ	0.0000	0.9999	0.0000
153	Target SciFi	π	0.0000	0.0070	0.9903
210	Target SciFi	e	0.9920	0.0000	0.0080
210	Target SciFi	μ	0.0000	0.9924	0.0072
210	Target SciFi	π	0.0001	0.0000	0.9998

The probabilities do not have to add to unity in each row. For example, $\approx$1% of electrons at 153 MeV/c are identified as both e and μ and the event is still read out. As shown, there is a large efficiency for identifying particles, >99%, with the exception of μ's at 115 MeV/c. As shown in the right panel of Fig. 25, there is overlap of the μ and π signals which leads to 2% of muons being rejected as pions using this scheme. This is an example of where optimization of the beam PID could lead to a higher μ efficiency at the expense of a small increase in π accidentals (which have a relatively small flux at this momentum).

In general the numbers reflected in Table VIII show the PID based solely on RF time from the beam SciFi is fairly clean. The situation can be even cleaner, especially at 115 MeV/c, by including the beam Cerenkov signals to take advantage of time-of-flight differences. Table IX shows that it takes the π's 8 ns longer than the μ's to travel from the IFP to the target at the lowest momentum. These time-of-flight differences can be used when a single particle types is identified as two types.

TABLE IX. Flight times and flight-time differences between IFP and target detectors. The β variations within the channel acceptance lead to time variations of up to 0.5 ns.

Momentum (MeV/c)	TOF$_e$ (ns)	ΔTOF$_{\mu-e}$ (ns)	ΔTOF$_{\pi-e}$ (ns)
115	36.7	13.0	21.0
153	36.7	7.8	13.0
210	36.7	4.3	7.4

Calibration of the beam PID system can, in principle, be done with bench tests, except for the relative timing of the RF signal, since the offsets between π, μ, and e signals and timing variations of the signals are calculable. Sending logic pulses into the electronics to mimic events, and by varying the offsets between the logic pulses, then allows the system programming and the response to single particles and accidental coincidences to be confirmed. The calibration will be adjusted and confirmed with data, since the time resolution available at the analysis level is at least a factor of two better than the resolution available at the trigger level. This is because the RF time phase relative to the detector signals is essentially arbitrary, being determined by cable lengths, and since the data itself allows the PID criteria to be fine tuned to optimize electron and muon acceptance while minimizing pion rejection. The calibration procedure can be done with a few hours of data.

One concern is the stability of the beam RF time. Past experience is that the beam RF time is very stable when the machine runs, but can shift by up to ≈100 ps when the machine goes down and is brought back up. Phase shifts of this magnitude change the efficiencies of Table VIII typically at the 0.1% level.

For determination of cross sections, while it is generally important not to lose statistics, which increases uncertainties, it is important to note that inefficiencies in the beam PID system do not change the absolute cross section. This is because the beam PID system both counts the beam flux and counts the μ or e signals that are sent to the trigger to take an event. There is a small effect in the absolute normalization from particles of one type being misidentified as another type, which leads to a correction determined in calibration runs. There is no effect on the relative cross sections.

VI. DAQ

A. Electronics and Readout

The experimental detectors mainly produce timing information to be read out through TDCs. We plan to use level discriminators and so require QDC information for pulse-height corrections to improve timing. This has been found in the case of the fast scintillators to be superior to constant-fraction discriminators. For the fast scintillators, two-dimensional comparisons of pulse size (dE/dx) vs. time have also proven effective for identifying particle types, even though the pulse size distributions overlap.

The needed readout channels for the experiment include:

- There are 196 scintillator PMTs, including 176 in the scattered particle scintillators, 12 in the beam monitor scintillators, and 8 in the veto scintillators. The anode signals are sent to discriminators, while the dynode signals are sent to QDCs.
- The SciFi detector has 3 planes of 40 fibers with double-ended maPMT readout, leading to 240 channels. The signals will be split to go to discriminators and QDCs.
- There are 9 channels for the beam Cerenkov. The signals will be split to go to discriminators and QDCs.
- There are 2850 channels in the straw chamber, with the signals sent to discriminators.
- The GEM chambers have an existing separate DAQ system, which has already been integrated into the MUSE MIDAS DAQ system. See Section III B 3.

In almost all cases, the analog signals will go to PADIWA boards.[5] The PADIWAs are custom-designed at GSI to provide a fast, compact and cost-effective readout for FAIR experiments. They provide 16 channels with $\times 10$ amplification, a level discriminator with independent thresholds for each channel, and a LVDS logic pulse output to the TRB3 boards. Additional lines on the cable connecting the PADIWA and TRB3 are used to

[5] For the beam monitor scintillators, the anode signals will first be sent to a constant fraction discriminator that is sent to the PADIWA board, to better monitor out-of-time signals.

control discriminator thresholds. Due to the different cabling and signals of the detectors, we are looking into modest customization of the PADIWA board inputs.

Each TRB3 has space for four interface cards that each manage and read out up to four PADIWAs. Thus, one TRB3 can control and read out 16 PADIWAs, or a total of 256 channels. The TRB3s each host five FPGAs. Four of the FPGAs control and operate each of the interface cards, and host the majority of the logic for the TDC and scaler information which the TRB3 produces for each channel. This leaves a central controlling FPGA mostly free for use in the construction of the trigger logic. The multiple functions of the TRB3 – scaler, TDC, and trigger logic module – reduces the cost of splitters, cables, and electronics by replacing independent scaler, trigger, and TDC modules.

As a TDC, the TRB3 system has achieved 11 ps resolution in bench tests,[6] which is sufficient for all MUSE detectors.

For use as a trigger, one TRB3 board will be outfitted to receive the fast trigger logic signals from each of the TRB3 boards in the system, to make the final trigger decision and distribute it to the other TRB3 boards and the non-TRB3 parts of the system.

The TRB3s are powered by a 48 V supply, and independently controlled and read out over gigabit ethernet. They require no VME crate. This will allow the TRB3s to be distributed throughout the experimental equipment, leading to shorter cabling, better timing, and hopefully reduced problems with ground loops. The system uses 23 TRB3s, including spares.

The MUSE test runs in πM1 have used a CAEN v792 QDC in our MIDAS DAQ to measure pulse sizes. Our baseline design is to use 22 v792s (including 2 spares) for the needed QDC readout channels. Since we have both positive and negative signals, we require the two different versions of the v792. To increase the readout speed of the DAQ, we plan to parallelize the readout, either with two split-backplane VME crates or four individual crates, each with five QDCs. The v792s will be read out in Chained Block Transfer mode in order to reduce the latency when reading the low occupancy MUSE events across multiple modules. We have tested the readout rates for an equivalent configuration and have shown that the estimated event rate is easily achievable using this

[6] In a test in πM1, we immediately achieved 40 ps resolution comparing a signal that was split and went through different numbers of NIM modules in each path to different channels on the TRB3. No effort has yet been made to test the limits of the system.

configuration.

In addition, the system will have input / output registers in each VME crate to distribute event numbers so that event alignment can be checked in the data.

B. Data Acquisition System

The 2012 and 2013 test runs used the PSI MIDAS system for data acquisition, which already supports the slow controls and standard data acquisition modules. The test system used an old Linux PC and a CES PVIC PCI bridge. The DAQ was operated at rates up to 2.4 kHz. MIDAS included support code for some of the modules we used, and we further developed code to support the CAEN v1290, which is very similar to the already supported v1190, and developed further v767 support code. In addition, our system had a CAEN v792 QDC and a v262 I/O register. In fall 2012, the TRIUMF ROOTANA code was adapted to analyze the data.

During our June 2013 test run, we enhanced our MIDAS DAQ with a new frontend to read out the GEM chambers with the MIDAS DAQ. A new analysis code, "MUSECOOKER," based on the GEM analysis being used for the DESY OLYMPUS experiment, was implemented. It also generates outputs that are examined with CERN ROOT.

In October 2013, new code was developed to pull the TRB3 data into the MIDAS readout, and we successfully read out and analyzed a few channels of data from one TRB3.

The TRB3s act as a nearly dead time free system, so the DAQ system rate capability is limited by readout of modules in VME crates. As discussed in Section III B 3, the current limits on the MUSE MIDAS DAQ in our tests have mainly been imposed by the initial implementation of the GEM telescopes at πM1. Reading out the two telescopes (only one will be used in the experiment) requires about 1.8 ms, limiting the rate to $\approx$400 Hz, but generating a data rate of $\approx$3 MB/s. Improvements of the GEM DAQ are underway, as outlined in Section III B 3. The readout of a v792, v1290, v1190, and v767 in a VME crate for the other detectors takes about 0.35 – 0.4 ms. Because this has not been a limiting factor in our tests to date, we have made no effort to use buffering or block readouts of these electronics, but will need to do so for the experiment.

C. Data Rates and Storage

A perfectly clean 100% efficient event would have

- 2 hits from the beam Cerenkovs,
- 6 hits from the 3 SciFi planes,
- 20 hits from the 20 wire chamber planes,
- 4 hits from the two planes of scattered particle scintillators,
- and no hits from the beam veto or monitor scintillators,

leading to 32 TDC signals and 12 ADC signals, not including the GEM chamber output. With ≈200 ns gates for the ADCs and TDCs, there is typically 1 background beam particle in each event, which typically neither scatters nor decays, leading to 10 more ADC and 10 more TDC signals. Thus, 2 kHz of triggers with no noise and pedestal suppression leads to an easily managed data rate of ≈0.6 MB/s – less for most of our kinematic settings – leading to about 16 TB of data for the experiment. As a result, the GEM system will likely remain the critical component limiting our DAQ rate capabilities and storage needs.

The data produced will be recorded on a new 90 TB RAID system and raw data will be copied to GWU for safekeeping. Analyzed data will be stored at all of the sites where MUSE data is under analysis *i.e.*, multiple U.S. universities.

VII. TESTS, COMMISSIONING, CALIBRATIONS, RUNS

The MUSE collaboration has performed beam line measurements, DAQ development, and equipment prototyping in three test run periods, during October - November 2012, June 2013, and December 2013. We continually assess from our findings what further activities are needed in advance of the experiment.

Our current expectations are for additional tests in mid and late 2014, related to beam tuning, SciFi and beam Cerenkov prototyping, simulations, and DAQ improvements. However, activities will focus on the start of experiment equipment construction once funding becomes available, which we expect will be in June 2014. We are currently engaged in more detailed planning for the staged arrival of equipment in late 2015, leading to a dress rehearsal run with essentially complete beam line detectors and one spectrometer in the last months of 2015.

A. Test Runs

A report on the 2012 beam tests is available [30]. Reports on the 2013 beam tests are in progress. Here we summarize some of the accomplishments and findings.

- Beam line:
  - Relative fluxes of different particle types were determined.
  - No significant differences were found in the beam size at the target or IFP for different particle types.
  - No significant differences were found in the beam dispersion at the IFP for π's and μ's.
  - A tune with a small beam spot at the target was found.
  - Significant backgrounds were found at the IFP (mainly neutrons and π's that decay before the target).
  - The use of a collimator at the IFP to limit the beam flux was found to produce fewer backgrounds than the use of the FS11 jaws before the first dipole magnet.
  - IFP to target time, RF time, and pulse-size data were used to identify small, percent-level, backgrounds in the beam.
- Equipment and DAQ
  - The MIDAS system was set up and data read out at up to 2.4 kHz for a few TDCs and QDCs.
  - Fast SC scintillators were successfully used to measure beam properties; QDC spectra agreed with simulations.
  - The OLYMPUS GEMS were installed, incorporated into the MIDAS DAQ, and used to measure beam properties.

- Sapphire and quartz beam Cerenkovs were prototyped, though not with the final PMT.
- A TRB3 was incorporated into the MIDAS DAQ and successfully read out.

• Other

- A mini-scattering experiment was attempted with one GEM telescope measuring the beam and one GEM telescope tracking scattered particles.

B. Installation and Dress Rehearsal Run

The aim of a dress rehearsal run planned for November 2015 is to test backgrounds and performance of the equipment in the experiment in a configuration as close as possible to how we plan to run. This requires commissioning of the equipment and development of a simplified trigger, as the run can be at low rate. Our goal is to have beam line detectors and (most of) one spectrometer in place. Setting up for the dress rehearsal run requires a staged delivery, installation, and commissioning of equipment during the ≈4 months preceding the test. The equipment available for the test and the arrival times will depend on the available money, and our current plans assume that the needed resources are available.

The first item needed is the detector support table, shown in Fig. 26. The GEM chambers are already at PSI and can be mounted on the table after it is set up in the area. A large number of scattered particle scintillators and the beam veto scintillators can be available much earlier than summer 2015, but will be brought to PSI taking into consideration convenience of shipping, storage, and commissioning and the need to be ready for the dress rehearsal run. The target Cerenkov and one element of the IFP Cerenkov should be available for installation and commissioning by August 2015. The SciFi detector is expected be available in September 2015. The beam veto scintillators will require a special mount as the scattering chamber is not expected to be available in 2015. The last item to arrive is the first straw chamber, planned for October 2015. Corresponding readout electronics will also be delivered to PSI in time to test the detectors. Staging the deliveries should allow intermixing installation and commissioning activities in the πM1

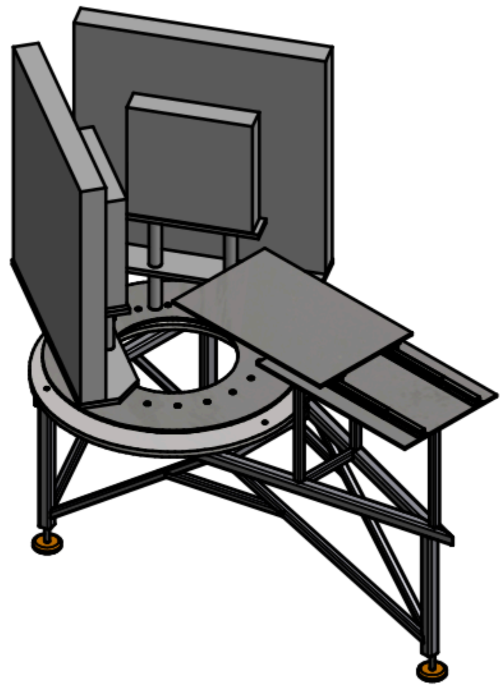

FIG. 26. Three-dimensional view of a preliminary design for a detector support table, also showing the straw chambers on the rotating panel. The cryotarget rises from the floor through a large central hole in the rotating panel and supports the veto scintillators. The beam Cerenkov, SciFi, and GEM chambers are mounted on the sliding table to the lower right. Other scintillators are on additional frames not shown.

area.

In general, the commissioning activities consist of measurements to determine optimal operating parameters – voltages and thresholds – for equipment along with debugging any issues found. Inherent in this is commissioning of the trigger and of the DAQ for readout and analysis of the data. Once the basic functionality is established beam line tests can be done. With detectors present, it will also be possible to take various measurements to validate the simulations, such as the multiple scattering by the detector elements and response of our scintillator walls to particles of various energies.

C. Calibrations

Several system calibrations are needed before we can take production data – some are not absolutely needed for the dress rehearsal run – including the following:

- Calibrate the absolute angle of the wire chambers.
- Calibrate the beam PID and trigger systems.
- Optimize the beam tune.
- Confirm the beam backgrounds in the as-built configuration to ensure that any extra shielding and veto scintillators improve the experiment.
- Determine the beam momentum.

Section II D describes how it is important to know central scattering angles at the mr level or better. As survey is standard, here we describe how the angle can be determined through data. Fig. 26 showed a support table for the beam line detectors and straw chambers. In the standard configuration, no beam particle can pass directly through the GEM chambers and the straw tubes. The table is designed so that the panel supporting the beam line detectors slides upstream, allowing the panel supporting the wire chambers to be rotated through a precisely determined angle, so that beam particles can pass through the GEMs and straw chambers, determining their orientation. The forward-angle part of the chambers can be rotated directly into the beam, and all of each chamber can be rotated into the beam in a "backward" configuration when the chamber is near 180°. Simple mechanical techniques can determine the rotation angle to $\approx$10 μm / 50 cm = 0.02 mr. The more important limits on angle determination from data are 1 mr intrinsic angle determination from the straw chambers, 0.4 mr intrinsic angle determination from the GEM chambers, and about 2 mr of multiple scattering for higher-energy particles in πM1, or somewhat over 2 mr in total. The chamber orientation can be determined to $\approx$10 times better than this, or about 0.2 mr, and confirmed with multiple measurements of the straw chambers at multiple angles with respect to the GEM chambers.

The beam PID was described in Section V B. Here we note that the performance of the beam PID system is easy, in principle, to determine by running with low-rate beam and triggering for all beam particles. The analyzed data checks that the system correctly identifies each particle type, and determines the efficiency for identifying a particle correctly and the inefficiency for identifying a particle as a different type. The system needs to be calibrated as a function of rate to make certain the effects of accidental coincidences are handled correctly, and that there are no issues that crop up in the FPGA programming with a high rate of inputs.

The trigger was described in Section V A. Its performance is verified through loose triggers during the data taking, but can also be studied through specialized tests; *e.g.*, pulser inputs into selected channels.

At each new energy it is important to verify and optimize the beam tune. The beam spot and divergence are monitored by the GEMs. The importance of knowing the beam momentum is discussed in Section VIII C 2, and the monitoring of the momentum with beam monitor scintillators was discussed in Section III B 4. Essentially, the time of flight of the e's, μ's, and π's over the $\approx$12-m flight path from the IFP to the target and the RF time, corresponding to the flight time over the $\approx$23.5-m flight path from the production target to the scattering target, can be used to determine the beam momentum at the $\approx$0.1% level. The RF time gives a longer flight path but with some uncertainty due to the different particle production processes.

D. Run Plan

Based on estimated beam fluxes, cross sections, and efficiencies, the experiment requires about 12 months of primary production beam time. We have not, at this point, tried to optimize the division of time between the various measurements, we have instead simply opted for 2 months of time at each of the 6 settings: 3 beam energies $\times$ 2 beam polarities. The order of the 6 kinematic settings is not crucial. Because there are possible long term changes in performance, we will likely change back and forth between kinematic settings in 2-week or one-month intervals. Within each setting we will alternate between production data, empty target background data, and no-target background data.

At this point we project that systematic point-to-point uncertainties will be larger than statistical uncertainties at smaller angles, but not at larger angles, so the optimization will vary depending on the scattering angle. As a further check on systematics, beyond the three primary settings, two identical spectrometers, and two beam polarities, we expect to take some data with the spectrometers slightly rotated in angle, rather than symmetric, and some of the run time at a beam momentum off by a few MeV/c from one of our 3 planned settings.

Detector efficiencies are expected to be high and measurable with the production data. For the GEMs and straw chambers, this is done with multiple redundant planes. The beam Cerenkovs and multiple SciFi planes provide efficiency checks for these detectors. There is no direct measure of scintillator performance, but the QDC spectra can be monitored, and loose triggers and scaler rates can be used to look for inefficient phototubes.

Random coincidence beam particles also provide an unbiased measurement of beam parameters, beam line detector performances, and their stability.

E. Manpower for Production Runs

Equipment installation and commissioning requires experts, but the MUSE production running will be done by the full collaboration. The collaboration currently includes about 45 physicists, but we expect the number to grow by about 10 once funding is approved, as groups recruit Ph.D. students and some additional postdocs to the project.

The MUSE production runs will last for about 6 months per year. We currently have a core group of nine senior personnel, and we expect at least one to be on site at all times during data taking. We plan for a core group of about 8 – 9 expert postdoc and Ph.D. students to rotate between their home institutions and PSI, and be the experts who are analyzing data and fixing problems. About 3 – 4 will be onsite at all times during the data taking. Other individuals in the collaborations will run 1 person shifts in the πM1 counting house, calling on the experts for accesses into the hall for problems and configuration changes. This requires these individuals to run about 2 weeks of shifts each year at PSI. In addition, we plan to configure the DAQ so that an individual at a home institution can run a near online replay to check data quality. This is done to halve the amount of travel needed.

VIII. ANALYSIS, CORRECTIONS, SYSTEMATICS, RESULTS

A. Data Analysis

1. Determination of Yields

Here we discuss various steps in the data analysis leading to the determination of yields. The event-data analysis will have as input the various QDC and TDC signals from the detectors along with trigger and beam PID information determined at the hardware level. From these raw data, assuming a clean single particle event, we will do the following:

- QDC spectra will be monitored to check for stability of detector gains, threshold setting, and consistency with simulations.

- Timing of all scintillators will be improved with QDC corrections to the TDC values. The scintillator and SciFi detector elements all have double-ended readout, allowing mean times to be determined. For the beam Cerenkovs, single-ended readout increases the expected $\approx$100 ps resolution by $\approx$50 ps (in quadrature) due to geometry.

- The GEM and straw chamber data will be used to determine tracks with of order 100 μm position and 1 mr angle resolution, from charge deposition in the GEM chambers and times in the staw chambers. The quality of the track can be checked with residuals since there are redundant tracking elements – for the GEM chambers this includes the hit position in the SciFi array. The tracks and detector redundancy are used to determine efficiency as a function of position.

- The incoming and outgoing tracks can be used to determine an interaction vertex, the quality of the reconstructed vertex, and the scattering and azimuthal angles. Resolutions are at the few mm level for positions and 10 mr level for angles, due to multiple scattering. Events reconstructed as not coming from the target can be removed.

- The tracks can be used to determine hit positions in the scintillators and the beam Cerenkov, which allows timing to be improved and path lengths to be calculated.

- The RF time is determined from the trigger, timed off the last beam line PMT hit. The beam line PMT signal times will be averaged to improve the RF time. The RF time and the time of flight between the IFP and target detectors identify the triggering particle type and check the beam PID system efficiency for identifying particle types.

- The speed β of the scattered particle can be calculated from the times and path length, allowing muon (pion) decays in flight to be separated from muon (pion) scattering events.

- Fiducial cuts will be applied to the GEM tracks, to be certain the trajectories point into the target liquid hydrogen volume.

- The data can be analyzed for accidental coincidences with other beam particles. Distributions in the SciFis and GEMs of these particles provide an unbiased monitor of the beam particle distribution stability, while time distributions of these particles in the beam line detector provide an unbiased monitor of the accelerator RF and channel momentum stability.

At this point relevant quantities have been determined, cuts can be applied, and counts can be summed up.

2. Removing Backgrounds

The estimated rates of the desired elastic scattering and background processes were estimated earlier and summarized in Table I; certain estimated count rates were shown in Fig. 4. Backgrounds are mainly removed through target reconstruction cuts and timing cuts, mentioned above and discussed in more detail below. Cuts on dE/dx vs. E from the scattered particle scintillators are helpful, but the difference in energy losses of π's, μ's and e's are not large compared to the statistical variations – see Fig. 20.

Cuts should be sufficient to remove π-induced events and nearly all muon decay events. Residual backgrounds, including scattering from the target end windows, can be subtracted with empty target runs.

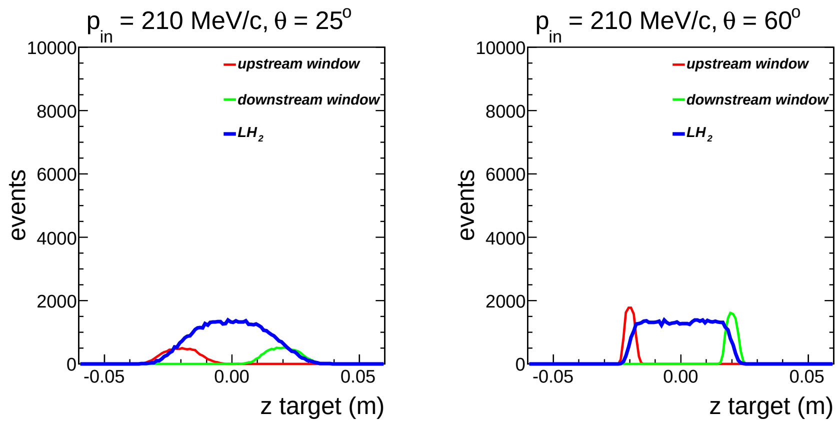

FIG. 27. Reconstructed interaction position along the beam line for two angles at a beam momentum of 210 MeV/c. The relative numbers of events are from Table I, but the absolute numbers are arbitrary.

3. Target Reconstruction Cuts

Figure 27 shows a simulated reconstructed image of the target along the beam line. The simulation included multiple scattering in the final GEM chamber, the vacuum and target entrance windows, the liquid hydrogen, the target and vacuum exit windows, and an estimated resolution (including multiple scattering) of the straw chambers. The simulation used a 4 cm long target cell with a 4 cm diameter, and a 0.125 mm kapton wall and 0.1 mm of super-insulation. The interaction position is found from the "intersection" of the incoming ray measured by the GEM chambers with the outgoing ray measured by the scattered particle chambers. We use a technique from proton polarimetry [31] of identifying the scattering vertex as the center point of the common perpendicular to the two rays – which is the minimum path between the rays. The simulation does not include the effects of energy loss slightly increasing multiple scattering as the particles propagate through the detectors and target, or curvature of the target windows.

While resolutions are at the mm level, the resolution of the interaction position along the beam direction varies mainly from a $1/\sin\theta$ geometric effect. The momentum dependence is weak. The relative scattering rate from the LH_2 and target end windows was shown in Figs. 4 and 5. The end cap scattering contributions have to be removed by background measurements and subtractions. Two techniques are available and we plan to use both. First, the background measurement is done on either the target cell with the hydrogen pumped out, or an identical empty cell. Second, the background measurement is done on $\approx 6\times$ thicker end windows, for the same multiple scattering as the target. Both techniques check the quality of the vertex reconstruction. With backgrounds about 30% as large as the signal, uncertainties are optimized by measuring the signal + background for $\approx$75% of the beam time, and the background for $\approx$25% of the beam time. However, the optimization has a shallow minimum and depends on angle and also on other residual backgrounds. The quality of the background subtraction can be tested on the known muon decay in flight events, discussed further below, and on the reconstructed target end windows at large angles, which are narrow.

4. RF Timing Cuts and Subtractions

The trigger-level particle identification discussed in Section V B is improved at the analysis level from QDC corrections, path-length corrections, and averaging of multiple beam elements. Here we consider in more detail the rejection of muon decay events near the target from the time of flight between the beam line detectors and the scattered particle scintillators. (Incident electrons lead to electrons in the detector, which are always $\beta \approx 1$, and which provide a timing calibration reaction for the detectors.)

The μ-induced events generally lead to μ's in the detectors for elastic scattering and e's in the detectors for decays in flight. Figure 28 show simulated time-of-flight spectra in the scintillators for the desired μp elastic scattering along with μC elastic scattering and μ decays with the decay electron detected. For simplicity these simulations ignored the slight momentum decrease of the scattered muons, which would increase the separation of scattering and decay events. The relative numbers of event types are based on the rate estimates shown in Fig. 5; in particular here we assume that the μ decay rate is already reduced a factor of several by z-target cuts of ± 5 cm. The muon decay rate itself can be essentially cleanly measured with a no-target run.

From Fig. 28 we conclude that scintillator timing generally separates μ scattering from the μ decays, but it is not able to distinguish between μC from μp scattering. Time-of-

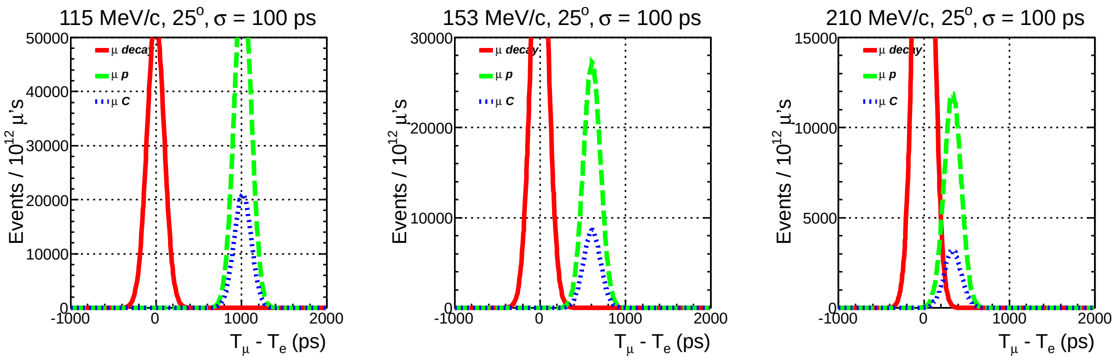

FIG. 28. Time-of-flight distributions for three beam momenta at an angle of 25°. The time of flight (minus the electron time of flight) was calculated from the target Cerenkov to the scattered particle scintillators, for particles scattering or decaying within ±5 cm of the target center. The 100 ps (σ) time resolution matches the expected resolution of the Cerenkov; the scintillator resolution should be 50 ps or less for each plane. The differences between the spectra for different angles are modest.

flight cuts reduce the decay muon rate by about 100%, 96% and 34% at 115 MeV/c, 153 MeV/c and 210 MeV/c, respectively, all while keeping the μ scattering inefficiency well below 0.1%. The remaining muon decay events and the μC scattering have to be measured and subtracted.

The subtraction of the μC events was discussed above in Section VIII A 3. Considerations for subtracting the μ decay events are similar. Subtracting a large number of decay events requires that the background and signal + background runs be for about equal amounts of time. Since only about 0.001% of the muons decay per cm of flight, the muon decay distribution is essentially flat except for the spectrometer acceptance. The distribution is also largely unaffected by the target being present or not, since to a large degree the decay electrons undergo only a small amount of multiple scattering. Thus the shape of the distribution outside the target region calibrates the correct normalization of the subtraction.

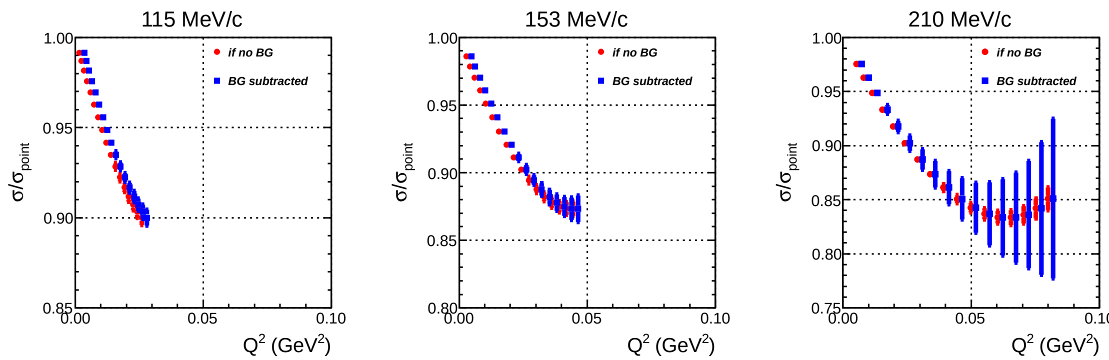

FIG. 29. Estimated statistical uncertainties for $\mu^+ p$ elastic scattering cross sections. The red points indicate the uncertainties that would be attained in one month runs at each momentum, assuming there is no background. The blue points show how the uncertainties grow from a one month measurement of the end cap scattering and μ decay backgrounds, which are then subtracted. If, *e.g.*, timing resolution is better than assumed, then the uncertainties will shrink towards those of the red points. Blue points are slightly offset to improve visibility. Each point corresponds to a $5°$ bin in scattering angle.

5. *Projected Data with Statistical Uncertainties*

Using the information given above, it is possible to take the run plan, the rate estimates for these processes, and the μ decay cut efficiency and work out the statistical uncertainties resulting from the yields and subtractions. This is shown in Fig. 29 for the positive polarity μp scattering. Because the larger μ decay background is efficiently removed by time-of-flight cuts at the lower momenta, the background only grows significantly for the 210 MeV/c data at larger angles. The statistical uncertainties are below the 1% level for nearly the entire 115 MeV/c and 153 MeV/c distributions, but generally above 1% at 210 MeV/c. (For negative polarity, the larger muon flux at 210 MeV/c reduces the uncertainties by about a factor of $\sqrt{2}$.) Figure 30 shows a similar plot for positron elastic scattering. Here, there is no large background and thus no need for the long background run, but the background run is determined by the μ scattering being done at the same time. The higher electron beam flux also reduces the statistical uncertainties. As a result, the background subtracted electron cross section statistical uncertainties are generally well below the 1% level.

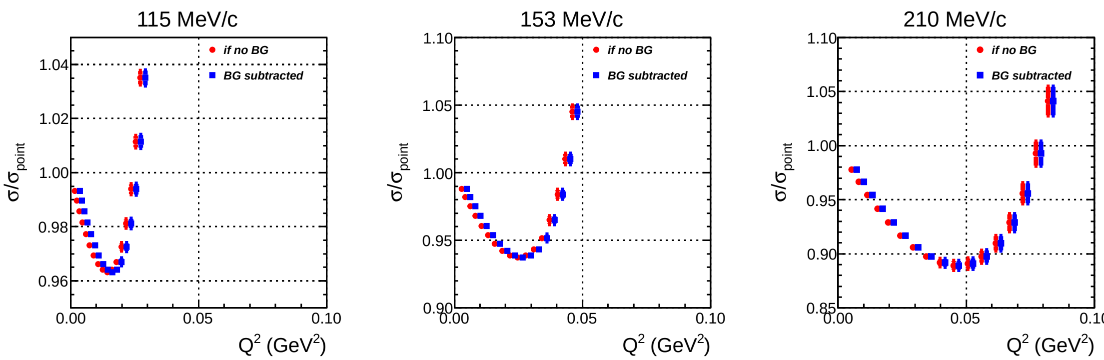

FIG. 30. Estimated statistical uncertainties for e^+p elastic scattering cross sections. The red points indicate the uncertainties that would be attained in one month runs at each momentum, assuming there is no background. The blue points show how the uncertainties grow from a one month measurement of the end cap scattering, which is then subtracted. Blue points are slightly offset to improve visibility. Each point corresponds to a 5° bin in scattering angle.

Recall from Table III that for electrons the negative polarity beam flux is greater, yielding smaller uncertainties, while for muons the negative polarity flux is lower.

6. *Derived Data with Statistical Uncertainties*

From the cross sections shown in Figs. 29 and 30, we will construct ratios to determine the consistency of the "electron" and "muon" form factors, and the size of two-photon effects.

Figure 31 shows the ratio of μp to ep elastic cross sections. It is not unity due to terms in the full cross section formula proportional to m/E and m/M_p, which are about 0 for the electron. We neglect this to show the relative statistical uncertainty in the cross section ratio, in Fig. 32. Ultimately, we will want to compare the electric form factor at the same Q^2, which will involve additional systematic uncertainties, as Q^2 is slightly different for the two projectiles and the magnetic contribution needs to be removed. The statistical uncertainty is reduced a factor of 2 in the form factor, compared to the cross section ratio, as $d\sigma/d\Omega \propto G^2$. It can be seen that the form factor ratio will have statistical uncertainties below 1% for much of our data set.

The cross section ratios of positive to negative polarity, or the cross section difference,

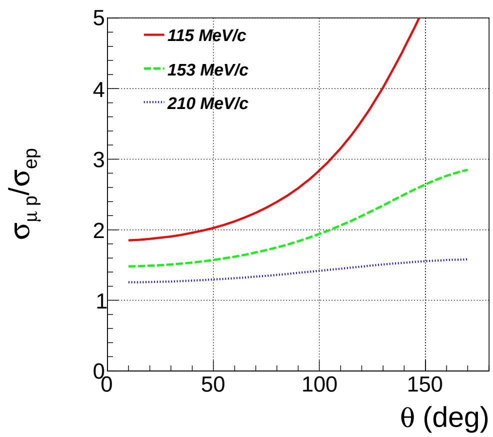

FIG. 31. Calculated ratio of μp to ep elastic cross sections at the same angle.

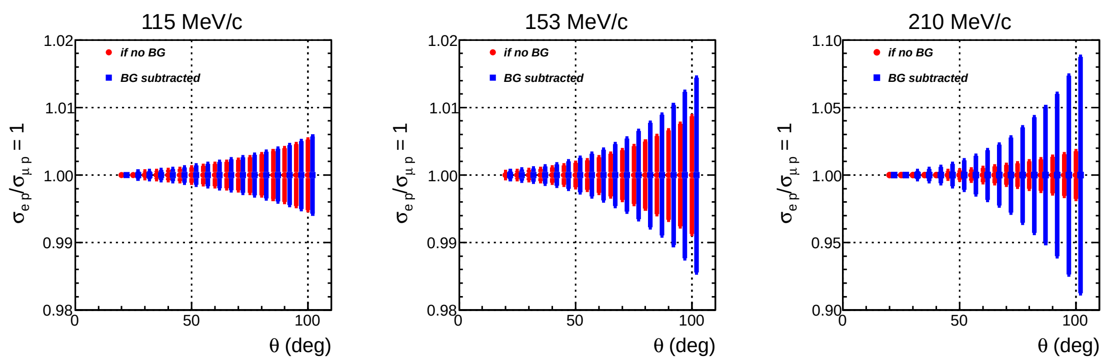

FIG. 32. Relative uncertainty in the ratio of μp to ep elastic cross sections. The relative statistical uncertainties in the form factors are half as large, since $d\sigma/d\Omega \propto G^2$.

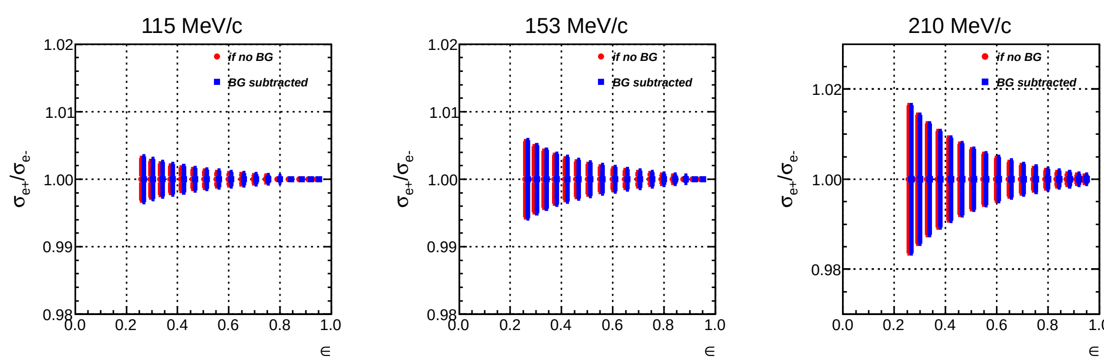

FIG. 33. Relative uncertainty in the ratio of e^+p to e^-p elastic cross sections.

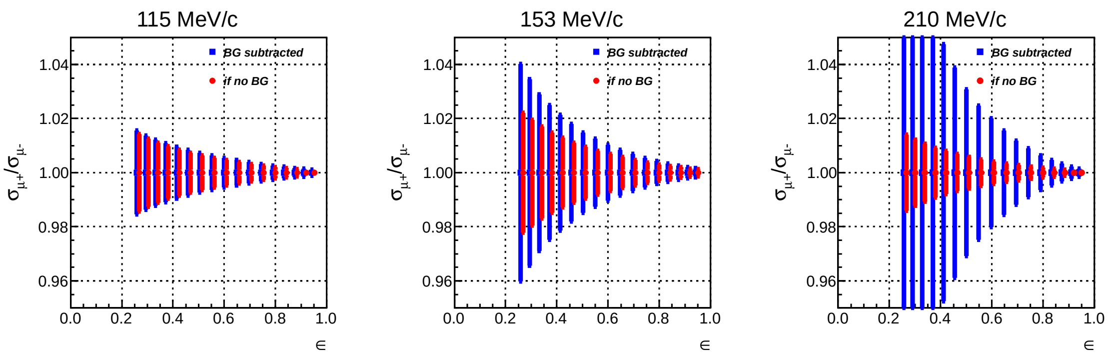

FIG. 34. Relative uncertainty in the ratio of μ^+p to μ^-p elastic cross sections.

yields the two-photon exchange contribution, which reverses sign between positive and negative polarities. The size of the effect is generally estimated to be about 1% – the ratio of cross sections will be about 1.02 – with a smooth decrease to 0 at $\theta = 0°$. The relative statistical uncertainties for the ratio of positive to negative polarity cross sections for electrons and muons are shown in Figs. 33 and 34, respectively. Here we plot as a function of the kinematic variable ϵ, the "polarization of the virtual photon", which ranges from 1 to 0 as θ changes from 0° to 180°. For electrons the uncertainties are small compared to the estimated size of two-photon exchange, while for muons the estimated uncertainties are mostly in the range of 50% - 100% of the estimated effect, for each data point.

B. Corrections

The μp cross sections determined from the background-subtracted yields must be corrected for a number of experimental and theoretical effects, and correction uncertainties must be evaluated. The experimental corrections in Eq. 1, included in Table II, are efficiency corrections. The procedures are all standard, and are all estimated to be small, so we do not discuss them further. Corrections for angle and energy offsets and averaging are also possible, with angle averaging most important as a correction. Uncertainties have been discussed and estimated in this report, but final uncertainties are determined in the analysis.

There are three types of more theoretical corrections we discuss here: two-photon exchange and Coulomb corrections, radiative corrections, and magnetic corrections.

1. Two-photon exchange and Coulomb Corrections

At very low Q^2, calculations of two-photon exchange (TPE) within a hadronic framework [35, 36, 37] are typically expected to be reliable, and are in good agreement with a low Q^2 TPE expansion [38], which is expected to be valid up to Q^2=0.1 GeV^2 and so covers our entire Q^2 range. However, even at low Q^2 the loop integral is over an infinite momentum range and TPE has uncertainties. Conventional, or soft, TPE calculations predict small effects on the MUSE cross sections. Afanasev's calculations of TPE shows an effect that approaches 0 at forward angles and increases with scattering angle. The effect is no more than about 0.2% in MUSE kinematics, with little difference between the correction for muons and for electrons, and estimated uncertainties about half of the correction. The effect has the opposite sign for positive and negative polarity beams, and will be measured in MUSE. TPE uncertainties dominate the uncertainty of all other radiative corrections for muons, but not for electrons.

Coulomb corrections can be thought of as a multiple-photon exchange correction in which the Coulomb force between the target and projectile accelerates the particles, causing the vertex kinematics to differ from the asymptotically calculated kinematics. Coulomb correction effects are small, but significant enough to be needed in extracting the proton radius. Standard codes exist.

2. Radiative Corrections

Radiative corrections procedures for electron-proton scattering are well established, and numerous codes exist. The important difference for muon-proton scattering is that the larger muon mass suppresses the emission of bremsstrahlung radiation. Care must be taken in adopting existing codes for MUSE, as some older codes assume the peaking approximation and / or the ultra-relativistic approximation ($m/E \to 0$). Afanasev has provided us with an exact calculation of the muon bremsstrahlung correction in MUSE kinematics. The correction is near 0 at $\theta = 0^\circ$, and grows with angle and beam momentum, becoming as larger as 3% for $\theta = 100^\circ$ at a beam momentum of 210 MeV/c. Afanasev estimates the uncertainty in the correction to be over an order of magnitude smaller than the correction, around the 0.1% level. The correction for ep scattering is about 5 times larger and similarly less precise.

3. Radiative Corrections and Beam Momentum

One aspect of the radiative corrections is that the beam momentum at the interaction point is degraded from the momentum out of the channel due to interactions with detectors before the target. This is referred to as energy loss, dE/dx, or external bremsstrahlung in different contexts. Thus the energy or momentum spectrum for the scattering must be calculated. We have done this using Geant4 with a flat channel momentum distribution and the planned SciFi and GEM detectors.

The beam momentum spectrum into and out of the target predicted by Geant4 is shown in Fig. 35. In each case, the initial spectrum was assumed to be a flat spectrum $\pm 1.5\%$ wide. The energy shifts are similar at the three beam settings, leading to larger fractional momentum shifts at the lowest beam momentum setting.

In Section II D, we used a simple flat distribution $\pm 1.5\%$ wide to investigate the effects of averaging over the beam momentum; Figure 7 showed that the effect was roughly 0.05% and independent of angle if one compares the average cross section to the cross section at the central momentum. We have repeated this procedure using the incoming momentum spectra shown in the left panel of Fig. 35; the result is shown in the right panel. The difference between the average cross section for all momenta and the cross section evaluated at the average momentum of the distribution is about $0.05\% - 0.1\%$, and the variation with angle is about 0.01%. Averaging over the full target will lead to a wider, more shifted distribution, with somewhat larger effects, but the basic result is that even if we use essentially the simplest possible analysis, calculating the average momentum, the resulting systematic offset will be at the 0.1% level, and nearly angle independent, so that the relative uncertainty is small.

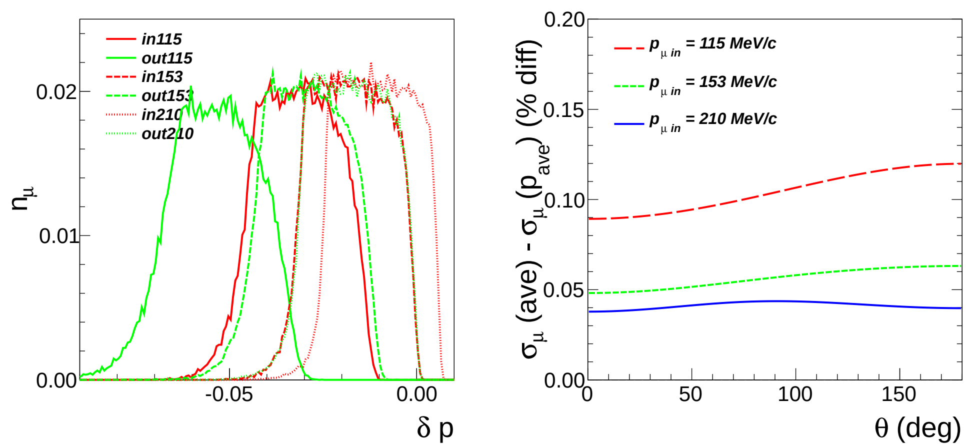

FIG. 35. Left: Momentum spectrum for beam muons entering and exiting the target. A fractional number of events per bin is plotted vs. the momentum relative to the central momentum of the πM1 channel. Right: Difference in cross section calculated for the average beam momentum and averaged over the spectra shown on the left.

C. Systematics

Systematic uncertainties were discussed in Section II D and summarized in Table II. There are uncertainties related to detector efficiencies, stability, and acceptance, uncertainties related to how well the kinematics are known, and uncertainties related to "theoretical" corrections, such as radiative corrections and magnetic contributions. A crucial point is that the absolute uncertainties cannot be determined precisely enough, so the experiment will use relative cross sections cross normalized to each other and to the Q^2 $= 0$ form factors. Thus, only the relative uncertainties need to be considered. Here, we review some aspects of the systematics in greater detail.

1. Beam Detector Related Systematics

Since beam line detector responses do not change the angle dependence of the cross sections, they do not affect the relative cross sections, and the related relative systematic uncertainty vanishes.

There is a small potential affect if the beam line detectors misidentify one particle type as another, since the different particles have interactions with different angle dependence. But the RF time separation between the different particle types is expected to be at or above the 10σ level in data analysis, so this should not be an issue. There is also a small effect from different momentum muons in the RF time tail of the muons, which might have effects at the $\approx$0.1% level, with smaller relative uncertainties, but is in need of further study.

2. Beam Momentum Determination Systematics

Figure 7 showed that the percentage cross section change is about $1-2\times$ the percentage beam momentum change, and the variation with angle is about an order of magnitude smaller. It also showed that averaging over a uniform $\pm$1.5% bin in momentum changes the cross section by $\approx$0.01 – 0.05%, with angle-dependent variations significantly smaller. Section VIII B 3 studied averaging with more realistic beam distributions generated from Geant, with similar results. We conclude that a beam momentum determination at the level of a few times 0.1% basically makes this systematic negligible.

The beam momentum can be determined by the TOF of particles from the IFP to the target ($\approx$12 m flight path) and by the RF time of particles at the target ($\approx$23.5 m flight path). A particle TOF determined with uncertainty ΔT determines the momentum to $\Delta p/p = (1+\beta^2\gamma^2)\Delta T/T$. In both cases cases, the e's have $\beta \approx 1$, and provide a calibration. The path lengths are known at the $\approx$ cm level, but the μ's and π's can also be used to determine both the path length and the momentum. Note that differences in production mechanisms of the particles could lead to differences in flight paths of particles from the M1 target at the $\approx$ 1 cm / 23.5 m = 0.04% level.

Resolution for peak determination for the momentum determination is about 25 ps, based on test run measurements with $\approx$300 ps wide timing peaks. Table X shows the quality of the momentum determination from TOF from the IFP to target. The RF time determination is similar. We conclude that RF time measurements are sufficient to determine the πM1 channel setting and beam central momentum at the $\approx$0.2% level, and the relative uncertainty is well below 0.1% for the cross section, and half as much for the form factor.

TABLE X. Estimated precision of momentum determination using TOF measurements from the IFP to the target region.

Momentum (MeV/c)	σ_p/p (%)
115	0.15
153	0.20
210	0.35

3. Target Systematics

The target thickness along the beam line is independent of scattering angle, so the systematic uncertainty vanishes. There is a small effect from the differing thicknesses of material that particles go through when scattering at different angles, that lead to slightly different amounts of multiple scattering, and can slightly affect the correction shown in Fig. 8.

4. Scattered Particle Detector Systematics

The scattered particle scintillator efficiencies were studied in Section IV B. The efficiencies are very close to 100%, except for ≈99% for e^+ due to positron annihilation, and can be studied through the QDC spectra and loose triggers. Due to the positrons, we assign a 0.1% relative systematic uncertainty to the scintillators. Associated with the scintillator efficiency are uncertainties from dead time corrections at the hardware level, including for individual scintillator paddles. The most forward, highest rate scintillator paddle, based on the simulations shown in Table VII, has a ≈90 kHz rate, leading to a dead time of ≈10 ns / 11 μs = 0.1%. Consequently there is a small uncertainty on the correction. All signals are scaled so that the dead time correction can be calculated.

The straw chambers each have 5 planes in each direction. A typical efficiency for straw chambers is about 95% geometric efficiency × 98% detection efficiency = 93% overall efficiency. Tracks require that 3 planes are hit, so tracking efficiency should be 99.99% for single track events. The efficiency can be monitored with the data, by seeing which straws do not fire when a track goes through them, and the relative uncertainty should be negligible. As indicated in Section II, the rates in the chamber are modest, and as long as high voltage and gas mix are stable the chamber performance should be highly efficient and stable as well. Thus, we expect that the systematics of wire chamber efficiencies are minimal.

The stability of the detectors should not add any significant relative uncertainty to the measurement, but this needs to be studied in the data analysis.

In determining the number of counts it is also important to determine the acceptance of each kinematic bin. As indicated in Section II D, the dominant uncertainty comes from the straw position uncertainty leading to a angular bin width uncertainty of about 25 μm / 2.5 cm = 0.1%. In the azimuthal direction, the bin width is about an order of magnitude more precise. There is also a contribution from the distance from the pivot to the chamber, which is determined by a combination of machining and survey at the level of $\approx$100 μm / 25 cm = 0.04% overall, with smaller relative uncertainties.

5. Electronics, Trigger, and Computer Live Time Uncertainties

There are a number of well known techniques for estimating electronic dead times and uncertainties. We plan to use two techniques: calculations based on pulse widths and measured rates, and sending in random pulses and measuring their propagation through the system to determine dead times. At the estimated beam, singles, and trigger rates the efficiencies should all be high and easily measured.

The most crucial issue here is careful programming of the trigger FPGA, which can introduce issues due to signal timing or high rates, if the code is not robust. There is no simple solution to this problem; code has to be developed and thoroughly tested. We will do so with calibration data at varying rates.

6. Uncertainties in Theoretical Corrections

As indicated in Section II D, Afanasev has now calculated radiative corrections for elastically scattered muons and electron in MUSE kinematics. The calculation makes no approximations, but does require some modeling for the two-photon calculation. Figure 36 shows some results. Soft two-photon exchange corrections are expected to be small. Overall radiative corrections are a few percent, with overall uncertainties about an order of magnitude smaller, and relative uncertainties at about the 0.1% level.

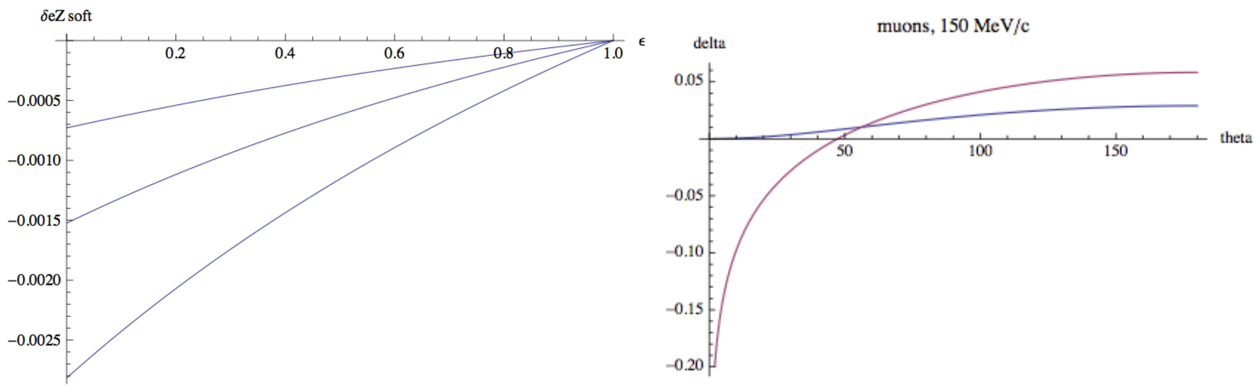

FIG. 36. Radiative correction calculations from Afanasev. Left: Soft two-photon corrections for the three MUSE beam energies as a function of ϵ. The correction grows with energy. Calculations shown are for electrons; the muon calculations are very similar. Right: Muon radiative corrections at 150 MeV/c for MUSE. The blue (red) curve is the full (approximate) calculation.

7. Analysis Uncertainties

Additional systematic uncertainties might arise from the analysis procedure and lead to relative uncertainties. Typically it is hard to estimate the size of these uncertainties in advance but it is fairly straightforward to estimate them from the data. Examples of possible issues include noise and / or backgrounds that might affect the ability of the code to correctly track, variations in extracted cross section with cuts of track reconstructions and times, and inconsistencies in results derived from alternate methods that should yield the same answer. Since the highest detector rates and the worst reconstruction of the target are for forward-angle detectors, there is a possibility that the systematics will be worse and more uncertain at forward angles.

8. Systematic Uncertainties for Ratios

We now consider what the systematic uncertainty is when we take ratios of cross sections to compare positive to negative polarity for two-photon effects or to compare electrons to muons for a lepton universality test.

In comparing electrons and muons, we want to make comparisons of cross sections and form factors at the same Q^2, not at the same scattering angle. Since the kinematics are not exactly the same for the two processes due to the different masses and the different dE/dx of the incoming particles in the detectors, most of the systematic uncertainties in Table II remain. The scintillator efficiency, angle determination, and multiple scattering uncertainties partially cancel since the change in angle for muons vs. electrons is not too large, and the shape of the correction is very similar in the latter two cases. The magnetic correction can be considered to cancel – since we are looking for differences between muons and electrons, it is sufficient to consider the magnetic contribution to be the same. We assume for now that the partially canceling systematics are about half as large for the electron to muon ratio, so that the relevant relative systematic uncertainties become 0.24% for muons, 0.55% for electrons, and 0.6% on the cross section ratio, or 0.3% on the electric form factor. For comparing electrons to muons the normalization uncertainty of 0.2% (0.1%) on the cross section (form factor) must also be considered, but the total uncertainties do not increase appreciably from 0.6% (0.3%).

In determining the two-photon effects, we take the ratios of cross sections of positive and negative polarity muons and electrons at the same beam setting, as well as can be done, and at the same scattering angle, but at different times. Thus the solid angle and angle determination uncertainties vanish, as do the non-two-photon part of the radiative corrections. Multiple scattering should also be essentially the same for the two beam polarities. What remains are the scintillator efficiencies (0.1%) since they can vary with time and polarity and the beam momentum uncertainty (0.1%). In addition, the normalization uncertainty of 0.2% remains for each cross section so that the systematic uncertainty on the ratio becomes about 0.3%. (Note that most calculations predict tiny two-photon effects at forward angles, which suggests that either the ratio can be renormalized to unity at forward angles, or that the difference from unity provides a check of the quality of the data.) There is a small potential effect since the relative numbers of each particle type are different in the two polarities, although the overall beam flux is the same, so detector rates might be slightly different. Thus the two-photon systematic uncertainties are very small, and statistical uncertainties will dominate.

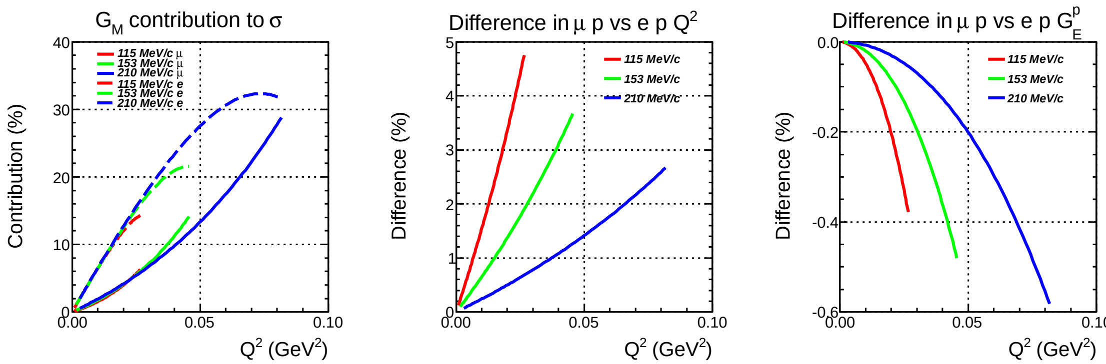

FIG. 37. Corrections related to extracting the electric form factor from the cross section for comparison at constant Q^2 rather that constant scattering angle. Left: Portion of the cross section coming from the magnetic form factor G_M. Solid (dashed) lines for for μp (ep) elastic scattering. Middle: Percentage difference in Q^2 between μp and ep elastic scattering at the same beam momentum and angle. Right: The difference in the electric form factor arising from the different Q^2. All estimates use the Kelly form factors.

To compare the electric form factors in the muon and electron case, corrections are made for the magnetic contribution to the cross section and for the Q^2 difference between μp and ep elastic scattering at the same beam momentum and angle. Figure 37 shows factors related to this determination. The magnetic contribution ranges up to about 30% at the largest angles. In the range of the MUSE experiment, fits of the Bernauer data *that fit the data well* suggest that the uncertainty in the magnetic form factor is no more than 0.3%. Including fits that do not fit the data well would triple this uncertainty. The uncertainty of the magnetic contribution to the cross section is then no more than about $30\% \times 0.3\% \approx 0.1\%$.

D. Radius Extraction

Here we provide projections for the extraction of the proton charge radius based on the run plan, statistics, and systematic uncertainties presented in this report. We have not yet attempted to fine tune the run plan. This projection, using equal time at each setting, thus represents a conservative estimate of the potential results.

The counting statistics are based on the following:

- Beam e, μ, and π fluxes as given in Table III, with the total beam flux limited to 5 MHz.

- The liquid hydrogen target is a 4-cm long cylinder, with a density of about 0.07 g/cm^3. The Kelly form factors [20] were used to estimate the scattering cross section.

- Target entrance and exit windows totaling 250 μm of kapton. Elastic cross sections were calculated with a parameterization of the carbon form factor used in [39] – the chemical formula for kapton is $C_{22}H_{10}N_2O_5$, so we expect that carbon elastic scattering is the dominant contribution. The oxygen form factor is roughly similar in shape to the carbon form factor, but falls faster with Q^2, while the hydrogen in the kapton foil amounts to about 0.3% of the hydrogen in the cryotarget. Quasifree scattering rates were estimated from the number of protons in the kapton, assuming equality of free and quasifree cross sections, and neglecting the neutron since G_E^n is small at low Q^2.

- Beam time is 2 months for each momentum at each polarity, with 1 month of signal measurements and 1 month of signal + background measurements which determine the end cap background for μ and e elastic scattering and the μ decay background.

In extracting the radius from a simple linear fit to the form factor, one can improve the extraction by minimizing the uncertainties or by increasing the Q^2 range to improve the sensitivity to the slope. However, as one includes data at larger Q^2 values, one has to worry about deviations from the simple linear fit yielding an error in the extracted slope. One can attempt to fit with more parameters, giving up statistical sensitivity to the radius, or to estimate and minimize the error made in the one-parameter fit.

Given the low Q^2 values of the proposed measurement and the fact that the larger Q^2 values have larger uncertainties, we have taken the latter approach, making a single parameter fit and making estimates of the 'truncation' error related to the use of a truncated expansion in the fit. The polynomial fit is not ideal for fitting, because the fit will always go to $\pm$ infinity in the region of large Q^2, while the form factor should become small. One can use an inverse polynomial, or other functional forms that have been suggested because of improved analytical properties or because they better decouple the radius from the higher-order terms, *e.g.* the continued fraction expansion [2] or the z-expansion [9]. We can examine these options for a final analysis, but to estimate the truncation uncertainty, we use the simplest of these 'well behaved' forms, an inverse polynomial. We perform the extractions based on input data according to a polynomial or dipole form and estimate the truncation error based on the largest deviation from the input. We believe that this can be further reduced with the improved functional forms mentioned above, but this will require more complete studies to obtain a convincing estimate of the truncation error, and so we use our estimate based on a simpler functional form to make what we believe to be a conservative estimate of the effect.

We propose to make two independent extractions of the radius from the data. Using only the lowest energy setting, $0.002 < Q^2 < 0.025$, the deviations from the single parameter fit are small and the extraction is limited by the experimental uncertainties. Combining the second and third energy settings allows for an extraction with much smaller uncertainties in the fit, but with a larger truncation error. For the lowest energy setting, we obtain a radius with a total uncertainty of 0.0170 fm, which is dominated by the 0.55% systematic uncertainty on the cross sections (as the statistics are much smaller for the low energy setting). From the 2^{nd} and 3^{rd} energy settings, we include a normalization factor for both data sets in the fit, such that the extracted uncertainty accounts for the possible difference in normalization between the two settings. The statistical and systematic uncertainties yield $\delta R = 0.0100$ fm, and we estimate that the truncation uncertainty is 0.0120 fm, yielding a total uncertainty of 0.0160 fm. Because these two extractions are dominated by different uncertainties, we take the combination of these two measurements as our final radius extraction, yielding an uncertainty of 0.0120 fm for the muon measurements. The improved statistics for positions and electrons do not help for the lowest energy setting, and make only a small difference for the higher energy measurements, yielding a 0.0110 – 0.0115 fm uncertainty for the electron and positron measurements.

Figure 38 shows the existing extractions along with the projections for our proposed measurements. We show results for e^+, e^-, μ^+, and μ^- separately, where we combine the radius extractions from the lowest beam momentum setting and the analysis from the high beam momentum settings. The left panel presents estimates of the absolute

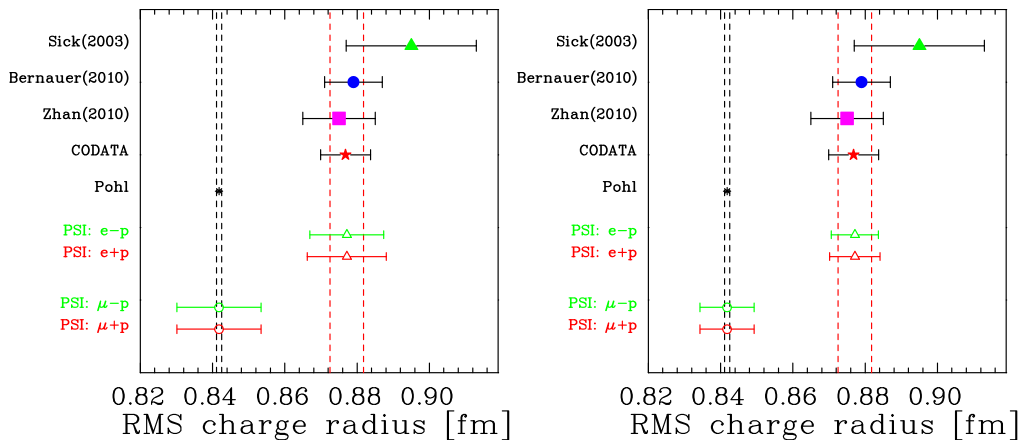

FIG. 38. Left: Recent extractions of the proton radius from electron and muon based measurements, along with the projected uncertainties from the proposed measurements. Right: The same recent proton radius results, but with projections for the *relative* uncertainties for the proposed measurements. See text for details.

radius determined independently in each case and the right panel presents the relative determination. The projected relative uncertainties are close to a factor of two better than the projected absolute uncertainties; this is discussed further below.

Note that we can combine the radius extractions from the $\mu^{\pm}$ and $e^{\pm}$ measurements. This improves the statistical uncertainty, but has little impact on the systematic uncertainty because many of the contributions (*e.g.* from any small angle offset or beam energy uncertainty) have a similar or identical effect for all of the different lepton beams. However, this means that in comparison of the different data sets, many of these systematics partially or completely cancel. So in isolating the two-photon exchange extraction from the comparison of e^+ vs. e^- or μ^+ vs. μ^-, or in the direct comparison of electron and muon scattering results, these uncertainties are significantly smaller. In addition, if we are making a comparison of two sets of measurements, rather than an extraction of the absolute charge radius, then the truncation error we make by performing a linear fit is not important. If the electron and muon data both give the same form factor, then the truncation error made in a linear fit will be in both the cases, and will not modify the comparison. There will be a very small difference in this effect, due to the slightly different distribution of the statistics in Q^2 for electrons and muons, but this difference is rather small.

So in the two-photon exchange or lepton universality tests, one can perform the simple linear fit of the entire data set to extract the radius. This yields a combined statistical and systematic uncertainty of 0.0075 fm (0.0065 fm for the electron data), and the truncation error is not relevant for these comparisons. Combining the results from positive and negative leptons yields a small improvement, as many of the systematic uncertainties will not be reduced in combining these data sets, yielding an uncertainty of 0.0070 fm and 0.0060 fm for the muon and electron results, respectively. This allows for an extraction of the difference between electron and muon radius extractions of $\delta R_{e-\mu}$=0.0090 fm, which would yield a 4.5σ measurement of a radius difference of 0.0400 fm, as observed in current measurements.

IX. COLLABORATION

Responsibility	Institution	Person
πM1 Channel	PSI	K. Dieters
Beam Cerenkov	Rutgers	R. Gilman (Spokesperson)
Scintillating Fibers	Tel Aviv	E. Piasetzky
GEM chambers (existing)	Hampton	M. Kohl
Cryogenic Target	George Washington	W.J. Briscoe
Wire Chambers	Hebrew	G. Ron (Co-Spokesperson)
Scintillators	South Carolina	S. Strauch
Trigger	Rutgers	R. Gilman (Spokesperson)
Readout Electronics and DAQ System	George Washington	E. J. Downie (Co-Spokesperson)
Radiative Corrections	George Washington	A. Afanasev
Software	MIT	J. Bernauer
Analysis Coordinator	Rutgers	K. Mesick
Simulations	South Carolina	S. Strauch
Project Manager	Rutgers	R. Ransome
Deputy Project Manager	George Washington	W.J. Briscoe

The MUSE collaboration is comprised primarily of people with experience in electron scattering experiments, some of whom have worked together for over 20 years. The collaboration has experience with experiments of the size and scale of MUSE, primarily electron and photon scattering experiments. The core of the collaboration at present can be viewed as the institutions taking a commitment to develop major parts of the experiment and / or obtain funding and / or have Ph.D. students and postdocs essentially fully committed to the experiment. A summary of commitments to the basic equipment development and other tasks is shown in Table IX. In addition, we are expecting Ph.D. students and / or postdocs focused on the experiment from GW, Hampton, Hebrew, Rutgers, South Carolina, and Tel Aviv. We expect these students and postdocs to be spending roughly half of their time at PSI during the roughly 2 1/2 year period that MUSE is installed and run.

At the time of this writing, a funding proposal has been sent to the US National Science Foundation for NSF / DOE consideration of funding the experiment. As part of the funding process, the collaboration formalized its structure by adopting a charter at its January 2014 meeting. Due to the size of the proposal, formal Project Manager and Deputy Project Manager positions have been added to our collaboration management structure.

---

[1] P. J. Mohr, B. N. Taylor, and D. B. Newell, Rev.Mod.Phys. **80**, 633 (2008), arXiv:0801.0028 [physics.atom-ph]

[2] I. Sick, Phys.Lett. **B576**, 62 (2003), arXiv:nucl-ex/0310008 [nucl-ex]

[3] R. Pohl, A. Antognini, F. Nez, F. D. Amaro, F. Biraben, *et al.*, Nature **466**, 213 (2010)

[4] J. Bernauer *et al.* (A1 Collaboration), Phys.Rev.Lett. **105**, 242001 (2010), arXiv:1007.5076 [nucl-ex]

[5] X. Zhan, K. Allada, D. Armstrong, J. Arrington, W. Bertozzi, *et al.*, Phys.Lett. **B705**, 59 (2011), arXiv:1102.0318 [nucl-ex]

[6] P. J. Mohr, B. N. Taylor, and D. B. Newell, ArXiv e-prints (2012), arXiv:1203.5425 [physics.atom-ph]

[7] A. Antognini *et al.*, Science **339**, 417 (2013)

[8] R. Pohl, R. Gilman, G. Miller, and K. Pachucki, "Muonic Hydrogen and the Proton Radius Puzzle," (2013)

[9] R. J. Hill and G. Paz, Phys.Rev. **D82**, 113005 (2010), arXiv:1008.4619 [hep-ph]

[10] R. J. Hill and G. Paz, Phys.Rev.Lett. **107**, 160402 (2011), arXiv:1103.4617 [hep-ph]

[11] B. Batell, D. McKeen, and M. Pospelov, Phys.Rev.Lett. **107**, 011803 (2011), arXiv:1103.0721 [hep-ph]

[12] V. Barger, C.-W. Chiang, W.-Y. Keung, and D. Marfatia, Phys.Rev.Lett. **108**, 081802 (2012), 3 pages, 3 figures. Version to appear in PRL, arXiv:1109.6652 [hep-ph]

[13] C. E. Carlson and B. C. Rislow, Phys.Rev. **D86**, 035013 (2012), arXiv:1206.3587 [hep-ph]

[14] C. E. Carlson and B. C. Rislow, (2013), arXiv:1310.2786 [hep-ph]

[15] D. Tucker-Smith and I. Yavin, Phys.Rev. **D83**, 101702 (2011), arXiv:1011.4922 [hep-ph]

[16] G. A. Miller, Phys.Lett. **B718**, 1078 (2013), arXiv:1209.4667 [nucl-th]

[17] W. Ruckstuhl, B. Aas, W. Beer, I. Beltrami, K. Bos, *et al.*, Nucl.Phys. **A430**, 685 (1984)

[18] E. Offermann, L. Cardman, C. de Jager, H. Miska, C. de Vries, *et al.*, Phys.Rev. **C44**, 1096 (1991)

[19] L. Camilleri, J. Christenson, M. Kramer, L. Lederman, Y. Nagashima, *et al.*, Phys.Rev.Lett. **23**, 149 (1969)

[20] J. Kelly, Phys.Rev. **C70**, 068202 (2004)

[21] J. Beringer *et al.* (Particle Data Group), “The Review of Particle Physics,” (2012)

[22] R.A. Schumacher and U. Sennhauser, “Particle Fluxes in πM1,” unpublished, 1987.

[23] M. Albrow, H. Kim, S. Los, E. Ramberg, A. Ronzhin, *et al.*, JINST **7**, P10027 (2012), arXiv:1207.7248 [physics.ins-det]

[24] R. Milner *et al.*, Nuclear Inst. and Methods in Physics Research A **741**, 1 (2014), arXiv:1312.1730

[25] P. Reimer *et al.*, Fermilab experiment 906, `http://www.phy.anl.gov/mep/SeaQuest/index.html`.

[26] E907 target web pages are at: `http://ppd.fnal.gov/experiments/e907/Targets/CryoTarget.html`.

[27] W. Erni *et al.*, The European Physical Journal A **49**, 1 (2013)

[28] M. Lutz *et al.* (PANDA Collaboration), (2009), arXiv:0903.3905 [hep-ex]

[29] R. Gothe, E. Phelps, R. Steinman, and Y. Tian, “CLAS12 Forward Time-of-Flight at USC: A Comprehensive Update”, Department of Physics and Astronomy, University of South Carolina, unpublished, November 2009, `http://www.physics.sc.edu/~gothe/research/pub/FToF12-review-11-09.pdf`

[30] W. Briscoe *et al.*, “MUSE Test Run Report,” Unpublished, `http://www.physics.rutgers.edu/~rgilman/elasticmup/testrun_report.pdf`.

[31] R.D. Ransome, “Measurement of the Free Neutron-Proton Analyzing Power and SPin Transfer Parameters in the Charge-Exchange Reaction at 790 MeV,” Ph.D. thesis, Los Alamos Report LS-8919-T, 1981.

[32] R. Ent, B. Filippone, N. Makins, R. Milner, T. O'Neill, *et al.*, Phys.Rev. **C64**, 054610 (2001)

[33] F. Weissbach, K. Hencken, D. Rohe, I. Sick, and D. Trautmann, (2004), arXiv:nucl-th/0411033 [nucl-th]

[34] A. Afanasev, I. Akushevich, and N. Merenkov, Phys. Rev. D **64**, 113009 (2001)

[35] P. Blunden, W. Melnitchouk, and J. Tjon, Phys.Rev. **C72**, 034612 (2005), arXiv:nucl-th/0506039 [nucl-th]

[36] P. G. Blunden and I. Sick, Phys.Rev. **C72**, 057601 (2005), arXiv:nucl-th/0508037 [nucl-th]

[37] J. Arrington, P. Blunden, and W. Melnitchouk, Prog.Part.Nucl.Phys. **66**, 782 (2011), arXiv:1105.0951 [nucl-th]

[38] D. Borisyuk and A. Kobushkin, Phys.Rev. **C75**, 038202 (2007), arXiv:nucl-th/0612104 [nucl-th]

[39] S. Boffi, M. Bouten, C. C. D. Atti, and J. Sawicki, Nuclear Physics A **120**, 135 (1968)